NATIONAL AIR INTELLIGENCE CENTER

SELECTED ARTICLES

DTIC QUALITY INSPECTED 2

19970206 017

HUMAN TRANSLATION

NAIC-ID(RS)T-0571-96   24 January 1997

MICROFICHE NR:

SELECTED ARTICLES

English pages: 109

Source: High Power Lasers and Particle Beams; pp. 313-319;
          327-341; 349-354; 367-372; 400-412; 440-447.

Country of origin: China
Translated by: Leo Kanner Associates
                F33657-88-D-2188
Requester: NAIC/TATD/Bruce Armstrong
Approved for public release: distribution unlimited.

TABLE OF CONTENTS

GRAPHICS DISCLAIMER

All figures, graphics, tables, equations, etc. merged into this
translation were extracted from the best quality copy available.

PHYSICAL DESIGN OF LINEAR INDUCTION ACCELERATOR CELL

Wang Huacen, Wen Long, Zhang Wenwei,
Yan Xiaolin, Deng Jianjun,
Ding Bainan, and Tao Zhucong

Institute of Fluid Physics
CAEP, P.O.Box 523
Chengdu 610003

ABSTRACT: Key aspects of the cell design of the linear
induction accelerator are presented. The equations of
the acceleration voltage and its flattop versus
cell parameters are given. The measures taken
to reduce the transverse coupling impedance of the cell
are described. Two prototype cells are also presented
as examples of the conceptual cell design.

KEY WORDS: linear induction accelerator, acceleration
cavity, wake and impedance, BBU instability.

1. Acceleration Voltage Amplitude and Width Design

A linear induction accelerator serves as an important
installation in accelerating heavy-current charged-particle
beams, and is widely applied in fields like flash x-ray
photography, plasma resonance heating, and heavy particle
inertially-constrained fusion testing. This accelerator has a

modular structure, i.e., its main unit is made up of numerous cells and corresponding pulsed-power systems in series connection. Undoubtedly, cell design plays a critical role in deriving high quality acceleration beam currents. To date, however, this topic has not yet been discussed in a general way. So this paper can be regarded as an preliminary attempt or trial effort in this field. The prototype cells presented here are intended for actual applications, with a working voltage of 250kV, voltage flattop ≥60ns, and acceleration electron beam current ≥3kA. Upon being accelerated through approximately 60 cells, the beam break-up growth factor is ≤20.

The fundamental function of the cell is to generate acceleration voltage with a particular shape and amplitude: the amplitude of the voltage is constrained by the pressure resistance of the insulation material as well as the acceleration gap breakdown field; and the shape of the voltage depends on the requirements for the quality of the accelerated beam current, and the kinds of particles that are accelerated. In the ferrite loaded core cell based on magnetic induction, an electric field with intensity E will be produced in the acceleration gap before a drive pulse ends or a core is saturated. This electric field can accelerate a charged particle beam when it is passing through a cell. In this case, the acceleration voltage of the cell is

$$U_c = \int_{l'} E dl' = -\int_s (dB/dt)/dS \qquad (1)$$

where l' is length of the electric field integrating loop; S is area of the core cross-section; and dB/dt is change rate of magnetic flux density. If this change is uniform in the entire core cross-section area S and the core is saturated at time τ, then $U_c \tau = \Delta BS$, where ΔB is the change of the total magnetic flux density within time τ, which is approximately twice the saturated core induction intensity B_s, i.e., $\Delta B \approx 2B_s$.

The ferrite ring we used had the value B_s=0.38T. After balanced consideration of factors, such as the beam tube and drift tube dimensions, the outer radius of the core, and leakage inductance, we selected the dimensions of its inner radius, outer radius and thickness, respectively, as d_0=508mm, d_i=237mm and δ=25.4mm. Eleven rings were placed in each cell with ΔB=0.75T, they can generate a voltage 250 kV and pulse width τ=S·ΔB/U_c=114.0ns. If an axial drive structure was adopted, the electrical length of the cell-generated core loaded axial line would be

$$T = l \, (\mu,\varepsilon,\mu_0\varepsilon_0)^{1/2} = 60l/c = 55.9\text{ns}$$

(2)

where l is core length; c is the speed of light in vacuo μ_r and ε_r, respectively, are core material versus magnetic conductivity and dielectric constant, which are 450 and 8, respectively; μ_0 and ε_0 are the corresponding in-vacuo values.

(a) accelerating cell with insulator   (b) accelerating gap without insulator
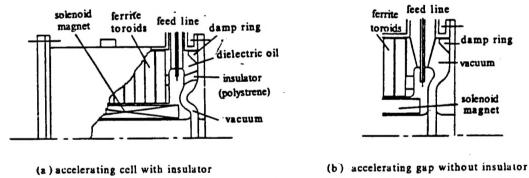
Fig.1 Schematic of the prototype cells

Fig. 1 is a schematic diagram of prototype cells. In Fig. 1(a), with the core placed in oil, the interface between oil and vacuum is a polystyrene insulation ring, which forms a 42^0 dip with the potential line of the acceleration gap. The electrons and the ring do not interact directly so as to avoid high voltage breakdown of the insulation material, which may be caused by charging or ultraviolet rays. The insulation ring can also be omitted, then in this case the core is placed in vacuo or we formulate an acceleration gap as shown in Fig. 1(b) as well as

3

another cavity, the acceleration gap of both being 19.5mm.

By using ELECAF2D and a program specially written by the present authors, the maximum field intensity of the stainless steel surface of the two acceleration gaps, respectively, was calculated as 18.9 and 18.5MV/m, while the maximum field intensity in the insulation ring was 7.0MV/m. It is predicted that there will not be an electric breakdown in a vacuum higher than 0.1mPa.

2. Approaches to Improving Acceleration Voltage Flattop

Fluctuations in the acceleration voltage flattop can give rise to increased energy dissipation of a beam current, and an overlarge energy dissipation can cause the beam current to lose the purpose of its application. Therefore, the change of the acceleration voltage flattop should be limited to $\leq \pm 1\%$. The cell of the linear induction accelerator and its drive loop can be equivalent to
Fig. 2. In Fig. 2, V_0 and Z_0 are Blumlein charged voltage and characteristic impedance; I_b is acceleration beam current; Z_f is core impedance; C_{gap} is acceleration gap and cell distributed capacitance, which works only at the rising edge or falling edge of the acceleration voltage and can be neglected in studying the voltage flattop; Z_c is external compensation loop impedance. Z_c should not only provide the drive loop with a matching impedance in the presence of beam current and under constant change of core bias, but also ensure that the core can obtain an appropriate reset current during Blumlein charging. At the same time, because of its compensation, the acceleration voltage flattop will also be somewhat improved. Of these parameters, Z_f affects the flattop most. From Fig. 2, the cell voltage can be derived as

$$U_c = (2V_0/Z_0 - I_b)(Z_f \| Z_c \| Z_0) \qquad (3)$$

It is known then that in the presence of compensation impedance Z_c, a change in Z_f will lead to a relative change in acceleration voltage U_c as follows:

$$\delta U_c / U_c = [\,(Z_f \| Z_c \| Z_0)/Z_f\,]\,[\delta Z_f / Z_f] \qquad (4)$$

If there is no compensation $(Z_c \rightarrow \infty)$, the corresponding change will be

$$[\delta U_c / U_c]_{Z_c \rightarrow \infty} = [\,(Z_f \| Z_0)/Z_f\,]\,[\delta Z_f / Z_f]$$

Obviously, this compensation can reduce the relative change of U_c, and the smaller the Z_c, the more remarkable the result can be. But if Z_c is overly small, large amounts of drive power will be consumed in the cell to heat the cell and will make the core reset current overly small, thus severely distorting the waveform of the acceleration voltage.
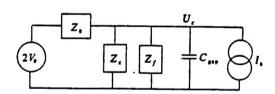
Fig.2 Equivalent circuit of the LIA cells
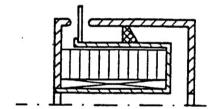
Fig.3 Schematic of the radial drive cell

If the beam current I_b has a change ΔI_b, then the relative change of acceleration voltage thus induced will be $\Delta U_c / U_c = -\Delta I_b / (W V_0 / Z_0 - I_b)$ whether or not there is Z_c. This indicates that a change of beam current can lead to a change in acceleration voltage that cannot be improved through compensation. In this case, it is extremely important to keep I_b stable during acceleration.

The compensation circuit can take different structural forms: either a resistance-capacitive or a resistance-inductance-capacitive network[1], or pure resistance, while the axial drive

5

cavity adopts an outside-cell resistance compensation box.

The core loaded cell has two drive modes: radial and axial. In the case of axial drive (Fig. 3), the core is partly equivalent to the total collected inductance

$$L = [\mu_r \mu_0 l / 2\pi)] \ln (R_0 / R_i) \qquad (5)$$

where l, R_0 and R_i, respectively, are the length, the inner radius and outer radius of the core; μ_r and μ_0 are similar to the designations in Fig. 2. Thus, $L=17\mu H$. At this instance, Z_f in Fig. 3 is the inductance resistance appearing in the cell. From Fig. 2, the acceleration voltage will decrease with the time t exponent, i.e.

$$U_c(t) = [2V_0 R / (R + Z_0)] e^{-t/\tau'}$$

$$(6)$$

where $\tau' = L/Z_{eff}$, $Z_{eff} = Z_0 \| Z_c \| R_b$, $R = Z_c \| R_b$; R_b is the beam loaded equivalent resistance under constant acceleration voltage and beam current. The definitions of Z_0 and Z_c are the same as in Fig. 2. Theoretically, this change of acceleration voltage can be compensated using a loop in which the impedance increases with the time exponent. However, as long as Z_0 has a larger value, such compensation will be extremely difficult to realize.

During axial drive (Fig. 1), the core can excite a current to enter along its central conductor, and the entire cell can be regarded as a magnetic coaxial line, which displays the characteristic impedance of pure resistance before the core is saturated

$$Z_f \equiv R_f = \{[(\mu_r \mu_0 / 2\pi) \ln (R_0 / R_i)] / [2\pi\varepsilon_r\varepsilon_0 / \ln (R_0 / R_i)]\}^{1/2}$$

$$= 60 (\mu_r / \varepsilon_r)^{1/2} \ln (R_0 / R_i)$$

$$(7)$$

where all the quantities are similar to those described above. By inserting numbers, we can obtain $R_f = 343\Omega$. It is known from Eq. (4) that at this instant, $\delta U_c = 0$ indicating that within a particular variation range of the core magnetic flux, the axial drive is good for deriving a better acceleration voltage flattop.

During the operation of a cell, the impedance should match

the output impedance of the pulse power system so as to avoid a high voltage reflection coefficient in the absence of beam current, to acquire a satisfactory acceleration voltage waveform, and to reduce the requirements for insulation from the system. From Fig. 2, when the impedances are matched, $Z_0=Z_f\|Z_c\|Rb=R_f\|Z_c\|R_b$. Then it is easy to solve

$$Z_c=[\,1/Z_0-1/R_b-1/R_f\,]^{-1} \tag{8}$$

From $Z_0=21.5\Omega$, and $R=250kV/3kA=83.3\Omega$, we can obtain $Z_c=31.7\Omega$. In the absence of beam current, the voltage reflection coefficient $(R_f\|Z_c-Z_0)/(R_f\|Z_c+Z_0)=0.15$.

Following each core drive, it is necessary to restore the magnetized state to the $|B_s|$ state before the next drive starts to generate another acceleration voltage pulse and realize the magnetic flux $\Delta B\approx 2B_s$ due to density change. Hence, the reset current I_I should be sufficiently large so that the outermost layer of the core can be fully reset, i.e., $I_t\geq 2\Pi R_0 H_s$. H_s is the core saturated drive field intensity (800A/m), so $I_t\geq 1.27kA$. This current can be provided by an independent circuit, yet in most cases, it is automatically provided by taking advantage of the Blumlein charging current. During charging, the change of tube potential in the Blumlein line is

$$U_b(t)=U_g C_g/(C_g+C)[\,1-e^{-\beta t}(\cos\omega t-\beta\sin\omega t/\omega)\,]\approx U_{g0}(1-\cos\omega t) \tag{9}$$

where $U_{g0}=U_g C_g/(C_g+C)$, $C=C_{B1}+C_{B2}$ and U_g are Marx output voltage; C_{B1} and C_{B2}, respectively, are Blumlein outer and inner water line capacity; $\beta=R_g/2L_g$, R_g and L_g, respectively, are charged resistance and inductance; C_g is impact capacity of Marx generator; $\omega=[(C+C_g)/C_g L_g C]_{1/2}$. Generally, $L_g\geq 50\mu H$, $R_g\approx 1\Omega$, and t is a few microseconds, so $e^{-\beta t}\approx 1$.
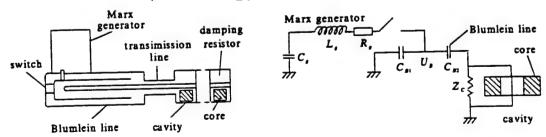
Fig.4 Core auto—reset in the cells driven by Blumlein line

7

From the foregoing discussion we know that $R_f \gg Z_c$; it can be tentatively assumed that the total reset current passes through Z_c. Hence,

$$I_{i} \approx C_{B2}dU_{a}/dt = C_{B2}U_{g0}\omega\sin\omega t$$

And the reset voltage is

$$U_{r}(t) = I_{i}Z_{c} = Z_{c}C_{B2}U_{g0}\omega\sin\omega t \tag{10}$$

The main switch starts acting at $t = \Pi/\omega$, and the reset magnetic flux $t = \pi/\omega$

can be derived as $\int_{0}^{\pi/\omega}U_{r}(t)dt = -2C_{B2}U_{g0}Z_{c}$, which should not be

smaller than the magnetic flux value by which the core can be reset to B_s, i.e., $2C_{B2}U_{g0}Z_{c} \ge (B_S + B_r)$, so

$$Z_{c} \ge (B_{s} + B_{r})S/(2C_{B2}U_{g0}) \tag{11}$$

where B_s and B_r are core-saturated induction intensity and remanance.

Of course, the reset current can be calculated even more accurately. From Fig. 4 and Eq. (9), the following can be derived:

$$d^{2}I_{i}/dt^{2} + (1/Z_{c}C_{B2})dI_{i}/dt + I_{i}/C_{B2}L = U_{g0}\omega\sin\omega t \tag{12}$$

The numerical results thus obtained are plotted as diagrams, which can be utilized whenever needed.

3. Lowering Cell Transverse Coupling Impedance

During acceleration, the relativistic charged particle beam interacts with the surrounding environments (beam tube, acceleration gap, bellows, deflection magnet, etc.) and radiates electromagnetic waves; these waves, always following the accelerated relativistic particles, are known as the wake field [2]. The field that is generated by the first particles acts on the follow-up particles and causes instability of beam current

8

movement. The quantity used to quantitatively describe the wake field is a function of wake field or coupling impedance, which refers to the same quantity expressed in the time domain or frequency domain. The coupling impedance is a feature of the acceleration structure and is not related to the property of beam current, and serves as one of the significant cell performance indicators. Once the coupling impedance of the cell is known, the buildup of beam current instability during acceleration can be derived from the initial property of the beam current and the additional transmission magnetic field. However, it is extremely complicated to calculate the coupling impedance of a cell that has even the simplest geometric shape and in this case, the calculations are expected to be conducted with the help of computer programs, such as Urmel and Mafia.

Like other linear accelerators, the linear induction accelerator suffers from the most critical instability, that is, beam break-up (BBU). Essentially, beam break-up stems from the fact that the beam current that deviates from the geometric axial line of the accelerator may excite, in the acceleration structure, a TM_{1n0} pattern electromagnetic field that imposes a transverse force on the follow-up beam current and that causes it continually to move in the transverse direction until it collides with the beam tube wall and is lost. The quantity used to evaluate the buildup of this instability is the transverse coupling impedance of the cell. The TM_{0n0} pattern field can increase the heat dissipation at the head of the beam current, and the extent of this effect can be assessed with the vertical coupling impedance of the cell.

In the linear induction accelerator, when the number of cells $N \geq 60$, the maximum transverse amplitude at the outlet of the beam current is

$$\xi = \xi_0 \exp(NZ_\perp \omega \rho I_b / I_a) \approx \xi_0 \exp[(1.16 \times 10^{-13} N I_b \omega Z_\perp)/B_s] \qquad (13)$$

where ξ_0 is the initial transverse amplitude of beam current;

$\rho=pc/B_se$ is the circular radius of the beam current particle in the magnetic field B_s, $B_s=0.13T$; c is the speed of light; p and e are total momentum and charge of particles; ω is TM_{110} pattern resonant frequency of the cell; in the cell shown in Fig. 1, $\omega=5\times10^9$/s; and $I_a=17\gamma\beta$ is Alfven current, kA; $Z_\perp$ is the transverse coupling impedance of the cell, which is only a function of frequency once cell structure is determined. The general goal of the accelerator is to require that $\xi/_0\leq20$. From Eq. (13), $Z_\perp\leq37.3\Omega$ is obtained. In many references, the transverse impedance is defined as $Z_\perp/c$, and accordingly, its value changes to 622Ω/m.

Eq. (13) implies that by increasing B_s, the effect of transverse coupling impedance can be reduced. Nevertheless, another effect in beam transmission, which is known as corkscrew movement, can restrict excessively intensified B_s. The TM_{010} pattern resonant frequency in the prototype cell is $\omega_1=3.6\times10^9$/s. On the other hand, according to the Urmel program, the vertical coupling impedance is expected to be $Z_1=12\Omega$. Let the change of beam current with time be $I=I_{b0}(1-e^{-\mu t})$, the following slow-down voltage will be generated in the cell:

$$V(t)\approx-(\mu I_{b0}Z_1/\omega_1)(e^{-\mu t}-\cos\omega_1 t)\qquad(14)$$

Since the beam current rise time is 20 ns, $\mu=1.1\times10^8$/s and the beam current amplitude is $I_{b0}=3kA$, the value in the first parenthesis in Eq. (14) is 1.1 kV, and the value in the second parenthesis reaches a maximum at $\omega_1 t=\Pi$, i.e., 1.76; therefore, $V(\Pi/\omega)=-1.94kV$. On attaining approximately 9ns, this voltage reduces to 1/e. Compared with the 250kV acceleration voltage, $V(\Pi/\omega_1)$ has a small effect and can only increase the energy dissipation at the beam head by 0.7%. The following discussion deals only with approaches to decreasing the transverse coupling impedance.

The key approach in decreasing the instability-caused beam break-up is to decrease beam current eccentricity. As long as

10

the principle of "combining three axes into one", i.e., beam
axis, magnetic axis, and geometric axis, can be realized, beam
break-up will not take place. To achieve this goal, it is
necessary to account for the cell mechanical design, focusing
spiral tube design, and overall configuration of the accelerator.

In addition, the beam tube should be smooth and flat, the
electrical conductivity of material σ should be large, and the
inner radius of the tube should be as large as possible. Because
the transverse impedance of the tube[5] $Z_{\perp p} \propto \sigma^{-1.2} b^{-3}$, and this value
will be increased if the inner wall of any tube is discontinuous.

By inserting a coaxial transmission line between the cell
and the beam tube, the strongest beam break-up mode can be
attenuated. A common LIA cell (Fig. 5) is a pill-box cell, i.e.,
the acceleration gap with width g can constitute a cylindrical
resonant cavity with a radius R_0, and on its both sides, there is
a beam tube with radius r_i. If it is changed to the shape as
shown in Fig. 5(b), then the electromagnetic wave in the resonant
cavity must first pass through a coaxial line with outer radius
r_0, inner radius r_i, and length 1 before arriving at the
acceleration gap d'. Therefore, by properly selecting the values
of r_0, r_i, and 1, the transverse coupling impedance of the cell
can be reduced. When R_0 is identical, the frequency of the two
cavities is identical, too. At this instant, mode TM:
$f^{a}_{mn0} = \mu_{mn} c / 2 \Pi R_0$; mode TE: $f^{e}_{mn0} = \nu_{mn} c / 2 \Pi R_0$.
μ_{mn} is the n-th root of the m-order Bessel function, while ν_{mn} is
the n-th root of the derivative of this function. The subscripts
m and n are mode exponents; c is the speed of light. When the
cutoff frequency of the coaxial line is $r_0 \approx r_i$, $r_0 - r_i \ll r_i$[6], for
mode TM: $f_{MC} \approx cn / [\Pi (r_0 - r_i)]$; for mode TE: $f_{EC} \approx cn / [\Pi (r_0 + r_i)]$. In
the prototype cell, $R_0 = 20$ cm, $r_0 = 10$ cm and $r_i = 8$ cm. Hence, when
n=1, $f_{EC} = 1.2$GHz, $f^{a}_{110} = 0.92$GHz. In other words, the beam break-up
mode TM_{110} must go through the attenuation of length 1 under the
cutoff frequency of the coaxial line before it can interact with

the beam current, which will greatly reduce the transverse
impedance of the cell.
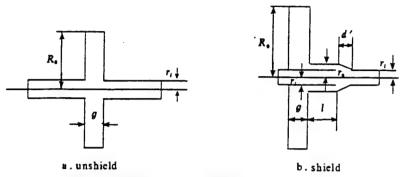
a. unshield   b. shield
Fig.5 Schematic of the unshield and shield cavities

The ferrite core can attract electromagnetic waves to a
great extent. In the prototype cell, the core is intentionally
exposed, and a ferrite half-ring is placed in the cell. At the
same time, eight measurement and drive holes are cut around the
cell, which are designed to let out the stored electromagnetic
energy through irradiation so as to reduce the transverse
impedance.

In the prototype cell with an axial insulation ring, the
ring is made of polystyrene, whose dielectric constant
(ε_{rp}=2.3~2.5) is close to that of the transformer oil (ε_r=2.3).
The electromagnetic wave, which transmits outward from the vacuum
tube, is incident at the insulation ring at an angle of arctg
$(\varepsilon_{rp}/\varepsilon_r)^{1/2} \approx 57^0$. The majority of this wave enters the oil zone and
is absorbed by the ferrite there.

The wider the acceleration gap, the smaller the beam tube
radius b, and the greater the transverse coupling impedance,
i.e.,
$Z_\perp \approx$ g/b. In the prototype cell, g=19.5mm and b=74mm, which have
been improved compared with the previous cells (g=45mm, b=73mm).
Besides, the symmetric drive of the cell, and the insulation ring
made as close to the beam axis as possible are good for reducing

12

the coupling impedance of the cell. If the inner surface of the insulation ring is coated with conductive material (on the condition that the pressure-resistant performance is not affected), $Z_\perp$ will also be greatly reduced. With all the foregoing approaches, it can be predicted from the Urmel program that, $Z_\perp=600\Omega/m$ in the cell with an insulation ring, and $Z_\perp=560\Omega/m$ in the cell without insulation ring. The experiment with $Z_\perp$ is still continuing.

To summarize, the two prototype cells presented in this paper can both meet the design requirements. The cell without an insulation ring can provide a lower coupling impedance, yet its heat dissipation appears poorer, and its working efficiency is not as high as that of the cell with an insulation ring, and, it is difficult to rarefy in this cell.

REFERENCES

1 Humphries S Jr. Principles of Charged Particle Acceleration. New York: John Wiley & sons, 1986

2 Chao A W. Coherent Instabilities of a Relativistic Bunched Beam. SLAC−PUB−2946, 1987

3 Heifects S A, et al. *Rev Mod Phys*, 1991, 63(3):631

4 Neil V K, et al. Further Theoretical Studies of the Beam Breakup Instability. *Part Accel*, 1979, 9:213

5 Caporaso J G, et al. Transverse Resistive wall Instability of a Relativistic Eelectron Beam. *Part Accel*, 1980, 11:71

6 Miller R B, et al. *J Appl phys*, 1988, 63(4):977

OPTIMIZING THE PROBLEM OF MATCHING
WAVEFRONT SENSOR AND WAVEFRONT CORRECTOR

Hu Zhaohui and Jiang Wenhan

Institute of Optics and Electronics
China Academy of Sciences
Chengdu 610209

ABSTRACT: In an adaptive-optics system, the effectiveness
of wavefront correction is influenced by the types of
wavefront sensor and corrector, their relative
configuration (matching) and wavefront reconstruction
algorithm. In this paper, computer simulation
experiments of a system using a Hartmann-Shack
wavefront sensor, a deformable mirror with continuous
surface plate and discrete actuators, and a direct slope
wavefront reconstruction algorithm were conducted. The
principle that each subaperture should be controlled
mainly by three actuators is derived.

KEY WORDS: adaptive optics, deformable mirror, wavefront
sensor, wavefront reconstruction algorithm.

0. Introduction

An adaptive optics system can be used in real-time
measurements of the dynamic errors of an optics system, and in
real-time the errors through feedback control it can correct so

that the optics system mentioned can operate properly. In this case, a wavefront corrector (tilting mirror+deformable mirror) and a wavefront sensor play a key role. Since the wavefront corrector and wavefront sensor contain a limited number of units, the subapertures of the sensor and the configuration of the corrector have an effect on the result of wavefront correction and the stability of wavefront control. Under such circumstances, configuration matching of the wavefront corrector and wavefront sensor becomes a problem.

In the adaptive-optics system simulation model (Fig. 1) that was constructed, a Hartmann-Shack wavefront sensor was utilized, together with several discrete actuators, a deformable mirror with continuous surface plate, and a direct wavefront slope control algorithm. With this model, the results of simulating several configurations were derived. The Hartmann-Shack sensor had 8x8, 10x10 and 11x11 subaperture arrays, while the deformable mirror had 54-88 units in triangular and square configurations. A comparison was also made of the fitting errors and conditional numbers in different configurations. In the simulation, two wavefronts to be corrected were applied, namely the Zernike wavefront mode and simulated atmospheric turbulence.

1. Principle

The Hartmann-Shack wavefront sensing principle is shown in Fig. 2. An array lens cuts the wavefront $W(r)$ into several subapertures; the beam in each subaperture is focused on the corresponding detector; by treating Δx and Δy, the aperture spot offset the quantities of the wavefront-to-be-detected versus the reference wavefront, the average slope of the subaperture along two crossing directions X and Y can be derived:

$$\begin{cases} S_{xi} = \dfrac{\Delta x}{f} = \dfrac{\int_{A_i} \dfrac{\partial W(r)}{\partial x}\, dr}{\int_{A_i} dr} \\[4mm] S_{yi} = \dfrac{\Delta y}{f} = \dfrac{\int_{A_i} \dfrac{\partial W(r)}{\partial y}}{\int_{A_i} dr} \end{cases} \tag{1}$$

where f is focal length of a sub-lens; A_i is area of the i-th subaperture.
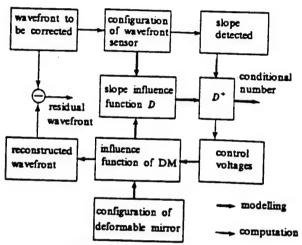
Fig.1 Block diagram of simulation

To solve minor errors or the control voltage of the deformable mirror through wavefront slope detection, we must carry out wavefront reconstructions. The very simple direct slope technique[1] was adopted in our simulation. If the wavefront slope, not the wavefront phase, was taken as a control quantity, then the wavefront slope may be viewed as a combination of several wavefront slope patterns.

$$\begin{cases} S_x(r) = \sum_{j=1}^{N} V_j S_{xj}(r) \\[4mm] S_y(r) = \sum_{j=1}^{N} V_j S_{yj}(r) \end{cases} \tag{2}$$

where $S_{xj}(r)$ and $S_{yj}(r)$ are the weighting factors of the j-th term wavefront slope pattern. If the j-th term wavefront slope pattern was defined as the wavefront slope generated by the j-th

17

actuator under unit voltage, then V_j was the voltage needed for the j-th actuator to generate wavefront slopes $S_x(r)$ and $S_y(r)$. $S_{xj}(r)$ and $S_{yj}(r)$ can be referred to as the slope influential factors of the j-th actuator; in this case, a simple and convenient wavefront reconstruction and decoupling technique can be obtained. The average wavefront slope of the j-th subaperture was detected as

$$S_{xi} = \sum_{j=1}^{N} V_i \frac{\int_{A_i} S_x(r)dr}{\int_{A_i} dr} = \sum_{j=1}^{N} V_i d_{xij}, \quad S_{yi} = \sum_{j=1}^{N} V_i \frac{\int_{A_i} S_{yj}(r)dr}{\int_{A_i} dr} = \sum_{j=1}^{N} V_i d_{yij} \tag{3}$$

where d_{xij} and d_{yij} are the average slope of the j-th slope influential factor in the i-th subaperture

$$d_{xi} = \frac{\int_{A_i} S_x(r)dr}{\int_{A_i} dr}, \quad d_{yi} = \frac{\int_{A_i} S_{xj}(r)dr}{\int_{A_i} dr} \tag{4}$$

Eq. (3) can be expressed in matrix form as follows:

$$S = DV \tag{5}$$

where D is the matrix of the slope influential factor with elements d_{xij} and d_{yij}, which depends on the deformable-mirror influential factors, on the wavefront sensor subapertures, and on the configuration of the deformable mirror actuators. It can be easily determined by using the adaptive-optics system itself. Wavefront slope vector S is the wavefront slope detected with the wavefront sensor in operation

$$S = [S_{x1}, S_{y1}, \cdots, S_{xi}, S_{yi}, \cdots, S_{xM}, S_{yM}]^T \tag{6}$$

where S_{xi} and S_{yi} are the average slopes measured along the X and Y directions; M is the number of subapertures; the voltage vector is

$$V = [V_1, \cdots, V_j, \cdots, V_N]^T \tag{7}$$

where V_j is the voltage needed for the j-th actuator; N is the number of actuators; $[...]^T$ is the transferred vector. The least-squares solution in Eq. (5) can be derived through the anomalous value resolution technique, i.e.,

$$V = D^+ S \tag{8}$$

where D^+ is the inverse of matrix D in a broad sense.

The deformable-mirror influential function can be defined as the normalized area-image change of the actuator under the action of voltage, which is normally fitted with a Gaussian function

$$f(r) = \exp\{-(|r|/\omega_0)^\alpha\} \tag{9}$$

where α is the Gaussian exponent and ω is characteristic width. In our experiment, the influential functions of two deformable mirrors developed at the Institute of Optics and Electronics affiliated with the China Academy of Sciences were measured. The result is: for the 19-unit deformable mirror, $\alpha=2.2$, $\omega_0=0.611d_0$; for the 21-unit deformable mirror, $\alpha=2.2$, $\omega_0=0.653d_0$, where d_0 is the central distance of the actuator. During the simulation, $\alpha=2.2$ and $\omega_0=0.63d_0$ were given with respect to Eq. (9).
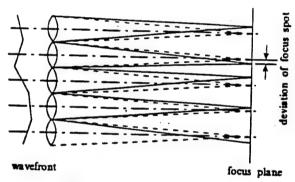
Fig.2 Hartmann-Shack wavefront sensor

Two kinds of wavefront to be corrected were employed in our simulation: the single-term Zernike polynomial and simulated turbulence. Table 1 shows the orders of the first 35 terms in the Zernike polynomials. For the n and m orders with the same radial and angular terms, the even number is of the $\cos m\Theta$ order, while the odd number is $\sin m\Theta$ order. Taking advantage of the Zernike spreading statistical characteristics of Kolmogorov turbulence[4,5], several random wavefronts resulting from atmospheric turbulence were derived and used as wavefronts to be corrected.

19

Table 1 Order of Zernike modes

radial degree(n)	azimuthal frequency/ m							
	0	1	2	3	4	5	6	7
1		1,2						
2	3		4,5					
3		6,7		8,9				
4	10		11,12		13,14			
5		15,16		17,18		19,20		
6	21		22,23		24,25		26,27	
7		28,29		30,31		32,33		34,35

To compare various configurations, two criteria were adopted, namely residual error and stability. Given a wavefront to be corrected W(r), the 101x101 lattice was sampled to calculate the average wavefront slope in the subaperture, and the voltage vector was computed from Eq. (8). The residual error after correction was

$$\Delta W(r) = W(r) - \sum_{j=1}^{N} V_j J_j(r) \qquad (10)$$

where $\Delta W(r)$ is the root-mean-square used as a criterion for evaluating the fitting capability.

In addition, the condition of matrix D $\mathrm{Cond}(D) = \sigma_{max}/\sigma_{min}$ was used as a criterion for assessing the interference resistance and stability of the system; σ_{max} and σ_{min} are the maximum and minimum anomalous value of D. The fluctuations of output voltage ΔV and noise in slope measurement ΔS are found in the following relationship:

$$\frac{\|\Delta V\|_2}{\|V\|_2} \leqslant \mathrm{Cond}(D) \frac{\|\Delta S\|_2}{\|S\|_2} \qquad (11)$$

where $\|\cdot\|$ is the Eulerian number. The greater the conditional number, the greater the fluctuations of voltage generated by ΔS; in fact, the conditional number is the degree of matrix ill-conditioning.

2. Result of Simulation

Seven configurations were applied in the simulation (Fig. 3). All the subapertures were in square configuration, including 8x8, 10x10, and 11x11 arrays (the central shield and four corners were removed) with a central shield 1/5. In schemes 3 and 4, the actuators were in square configuration, while in the remainder of the schemes, the actuators were in triangular configuration. The number of actuators and subapertures in these configurations is listed in Table 2.

Table 2 Number of subapertures and actuators in the simulated schemes

		1	2	3	4	5	6	7
Subapertures of sensor	configuration number	square 72	square 88	square 68	square 48	square 72	square 48	square 48
actuators of mirror	configuration number	Triangle 72	Triangle 72	Triangle 98	Triangle 68	Triangle 80	Triangle 54	Triangle 58

TABLE 3. Conditional Numbers

Table 3 Conditional numbers

scheme	1	2	3	4
Cond(D)	6.15	8.01	131.04	1028.6

scheme	5	6	7
Cond(D)	19.81	48.27	12.56
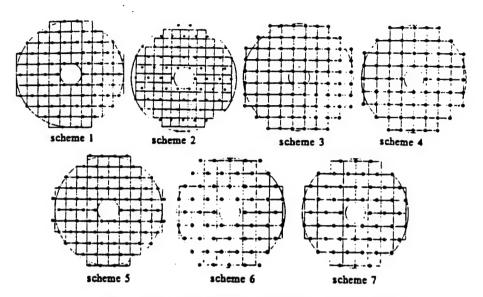
Fig.3 Configurations of subapertures and actuators in the simulation
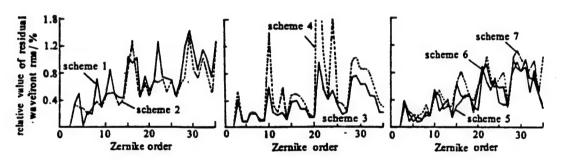
Fig.4 Residual errors for the first 35 terms of Zernike polynomial

The conditional numbers of various configurations in the
simulation are shown in Table 3. The residual errors for the
first 35 terms of the Zernike polynomial are given in Table 4,
where the abscissa gives the Zernike-mode order and the ordinate
is the ratio between the rms of residual wavefronts and the rms
of the given modes. In the simulation, several random wavefronts
of Kolmogorov turbulence were generated, the corrected residual
errors being shown in Table 4 in units of $(D/r_0)^{5/6}\lambda$, while r_0 is
the Fried constant. Additionally, the percentage of residual
error is also in Table 4.

22

TABLE 4.   The Residual rms Wavefront for Correcting
Kolmogorov turbulence $(D/r_0)^{5/6}$ - 1-3/4"

Table 4 The residual rms wavefront for correcting
Kolmogorov turbulence $(D/r_0)^{5/6}$

scheme	before correction	1	2	3	4	5	6	7
rms	0.1606	0.0165	0.0128	0.0075	0.0099	0.0087	0.0084	0.0095
%	100	10.3	8.0	4.7	6.2	5.4	5.2	5.9

Zernike mode No. 3   Zernike mode No.10   Zernike mode No.13
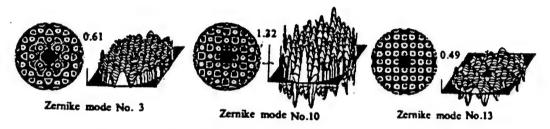
Fig. 5. Residual wavefronts of Zernike mode 3,
mode 10, and mode 13 corrected by scheme 4

3. Discussion

(1) The conditional number is extremely great in square
configurations (schemes 3 and 4) indicating that the matrix is
very sick. Fig. 5 shows the residual error after Zernike modes
3, 10, and 13 are corrected by the square configuration, which
clearly displays a checkerboard pattern. This is because this
configuration contains two mutually crossing but mutually
independent networks, and neighboring actuators belong to

23

different networks. When a small amount of noise is inserted in the slope, it causes the output voltage to fluctuate considerably.

(2) In some Zernike terms (No. 3, 10, 21 terms), the residual errors are remarkable and even greater than 1, suggesting that some Zernike terms are not suitable for correction, because there is coupling and confusion[6] in the modes. Obviously, some Zernike modes cannot be fitted with the combination of actuator influential factors.

(3) The conditional number of the triangular actuator configuration is smaller than that of the square configuration, particularly in the case when two actuators are located at the corner of the subaperture, and a third actuator is located in the middle of the diagonal (schemes 1, 5, 6, and 7). This can be explained with the principle of three points determining a plane.

(4) The edge actuator plays an important part in fitting errors. The residual error in scheme 1 is two times larger than that in scheme 5, their only difference being that there are eight more actuators at the edge of scheme 5. Scheme 6 has four more actuators at its edge compared with scheme 7, which, however, are far from the subaperture and as a result, its conditional number is four times as much as in scheme 7.

The simulation suggests that schemes 5 and 7, with smaller residual errors and better stability, prove to be better schemes.

REFERENCES

1   Jiang Wenhan and Li Huagui. Hartmann—Shack wavefront sensing and wavefront control algorithm. *Proc. SPIE*, 1990, 1271: 82

2   David I Fried. Least—square fitting a wavefront distortion estimate to an array of phase—difference measurements, *J.O.S.A.* 1977, 67(3): 370

3   Jan Hertmann. Least square wavefront errors of minimum norm. *J O S A* 1980, 70(1): 28

4   Robert J.Noll. Zernike polynomials and atmospheric turbulence. *J O S A* 1976, 66(3): 207

5   Nicolas Roddier. Atmospheric wavefront simulation using Zernike polynomials. *Opt Eng* 1990, 29(10):1174

6   Jan Hertmann. Cross coupling and aliasing in modal wavefront estimation. *J O S A* 1980, 71(8): 989

DESIGN OF RF CAVITY FOR HEAVY-ION-RESEARCH-
FACILITY-IN-LANZHOU COOLING STORAGE RING

*Zhang Wenzhi and Ye Feng, and
#Qin Jin

*Institute of Modern Physics
China Academy of Sciences
P.O.Box 31
Lanzhou 730000

#Institute of High Energy Physics
China Academy of Sciences
P.O.Box 918
Beijing 100033

ABSTRACT: A ferrite loaded RF (high frequency) cavity
for the Heavy-Ion-Research-Facility-in-Lanzhou (HIRFL)
Cooling Storage Ring (CSR) was designed through
calculation of two-dimensional RF electromagnetic fields.
The main parameters of the RF system and the distribution
of acceleration electric fields are obtained.

KEY WORDS: accelerator, heavy ion, ferrite loaded cavity.

0. Introduction

The Heavy-Ion-Research-Facility-in-Lanzhou Cooling Storage
Ring (in brief, HIRFL-CSR) is a synchrotron accelerator and a
cooling storage ring. In the synchrotron accelerator, the
charged particles execute circular movement around a fixed orbit,

its dominating magnetic field being distributed in a ring-shaped zone surrounding the central orbit, around which particles are in circular movement. Here, the frequency of the acceleration voltage is identical to the circular frequency of particles, or equal to an integral multiple thereof. The dominant magnetic field varies with the time period so as to ensure the resonant acceleration of particles. With increase in ion energy, the RF frequency increases; when particles reach the level of producing energy, the RF frequency attains its maximum value.

In electron or proton synchrotron accelerators, due to their extremely high incident energy, the RF system does not require conversion, or requires a minor conversion, while in a heavy ion synchronous accelerator, since ion has a low incident energy, its frequency varies over a wide range, and it requires a conversion, normally as much as a factor of approximately 10. Generally, the accelerating equipment used in this accelerator employs a ferrite loaded coaxial resonant cavity[1]. The resonant frequency of the cavity is changed by changing the magnetic material of the ferrite.

The conventional RF cavity design technique involves reasonably simplifying the cavity using the transmission line theory, i.e., converting a three-dimensional problem into a one-dimensional problem. In this case, the distributive parameter is made equivalent to the inductance, capacitance, and resistance of the lumped parameter, and the problem is simplified through mature circuit theoretical calculations. However, this technique accounts for only the one-dimensional situation, and it can hardly provide two-dimensional electromagnetic field distribution.

1. Design Theory and Acceleration Principle

For accelerator cavities with symmetry, two-dimensional

27

fields can be calculated, i.e., by solving a set of Maxwell's equations, the distribution of electromagnetic fields in the cavity can be derived, and accordingly, RF parameters can be calculated. In fact, Maxwell's equations can arrive at analytical solutions only in few cases, while in most cases, only numerical solutions can be obtained through numerical calculations due to the complexity of boundary conditions.

In structures with rotating symmetry, the electric field intensity E and magnetic field intensity H are not related to Θ. From Maxwell's equations, the following wave equation can be derived:

$$\nabla \times (\nabla \times H) = k^2 H \tag{1}$$

In columnar coordinates, for the time-varying TM mode or the TEM mode, only H_θ, E_r, E_z or H_θ, E_z are not zero. From Eq. (1), the scalar Helmholtz equation can be derived

$$\nabla^2 H_\phi(z, r) + k^2 H_\phi(z, r) = 0 \tag{2}$$

$$E_z(r, z, t) = \frac{1}{kr} \frac{\partial}{\partial r} [rH_\phi(z, r)]\sin\omega t \tag{3}$$

$$E_r = -\frac{1}{k} \frac{\partial^2 H_\phi(z, r)}{\partial z^2} \tag{4}$$

Through discretization of the foregoing Holmholtz equation with H_0 as a computational quantity, the discrete equations can be obtained

$$\sum H_\phi(V_n + k^2 W_n) = 0 \tag{5}$$

where $k^2 = \omega^2 \mu \varepsilon$, ω is the circular frequency of the RF system; n is the number of nodes that divide a lattice; V_n and W_n are functions of individual nodal coordinates. By solving the eigenvalue equations, the eigenvalue, i.e., the intrinsic frequency can be obtained, whose characteristic parameters, such as stored energy, average acceleration field, power dissipation, circuit impedance and merit factor can be calculated with corresponding formulas.

The RF system of the accelerator is composed of three parts: RF accelerating cavity, RF power supply and low-level control loops (including three loops, namely automatic frequency modulation, phase stability and amplitude stability). The charged particles are accelerated through the RF cavity generating an RF electric field versus time, while the circular frequency of particles at the central orbit is determined by the dominant magnetic induction intensity, their relationship being as follows[2]:

$$f_c = 1.43 \times 10^4 \frac{B_0}{\sqrt{\varepsilon_0^2 + (300 B_0 r_0)^2}} \frac{r_0}{R} \tag{6}$$

where r_0 and R, respectively, are the radius of curvature and average radius of particles at the central orbit in the bending magnetic field, m; B_0 is magnetic induction intensity at the central orbit, Wb/m; ε_0 is the stationary energy of particles MeV; f_c is circular frequency, MHz.

The increase in the dynamic energy of particles must stay in a particular relationship with the change rate of the dominant magnetic induction intensity to ensure that particles can move along a fixed orbit, its relation being

$$GV_a \cos\varphi_s = 2\pi r_0^2 \times 10^{-6} \frac{R}{r_0} \frac{dB_0}{dt} \tag{7}$$

where G is the times of acceleration that the particles experience in one cycle; V_a is amplitude of acceleration voltage; ϕ_s is the equilibrium phase angle of particles.

The dominant magnetic field changes periodically. Each time when the magnetic field changes from low to high, one particle beam will be accelerated to its final energy. It is through the accurate changes of the RF electric field intensity and the dominant magnetic induction intensity that the synchrotron accelerator can ensure a resonant acceleration of particles.

2. HIRFL-CSR RF Cavity Design

The overall HIRFL-CSR design requires that the particle circulation frequency of the RF system[5] be f_0=0.208-1.9MHz; the number of accelerating harmonic waves be h=7; the number of stacking harmonic waves be 7, 14, 28, 30; the RF frequency be f=1.53-13.54MHz; the peak voltage be V_a=7.2kV and the aperture of beam current be r=100mm.

In selecting ferrite material for loaded cavities, the major factors to be considered include its magnetic conductivity μ_r, dielectric constant e_r as well as the effect of temperature, electric field, and magnetic field. The heavy ion synchrotron accelerator requires magnetic material with high magnetic permeability and low RF dissipation, because the frequency of its acceleration system changes over a wide range. To design a cavity with stable operating capabilities, and to prevent the ferrite material from being subject to a "figure of merit" effect[3] in a RF electromagnetic field, the stored energy should not exceed the threshold value $(3\pm1)\times10^{-7}$J/cm^3[4], and the RF magnetic flux should be limited below 10mT.

Figs. 1 and 2, respectively, show the electric field distribution in the RF cavity, and the electric field distribution in the accelerating gap. In Fig. 2, the central frequency is 1.397MHz; the cavity dimensions OD0.66x2.55m. The loaded impedance of the RF cavity decreases with the increase in frequency, while the RF power dissipation increases with the increase in frequency with a maximum value 60kW as shown in Fig. 3. The resonant frequency of the cavity increases with the decrease in μ_r value of the ferrite material in a relationship as shown in Fig. 4. Fig. 5 shows the figure of merit of the cavity versus frequency. In our calculations, the μQF curve of the ferrite material was derived from reference [7], and the gap capacity C=250.2pF.
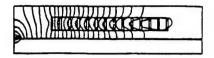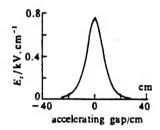
Fig.1 Electric field in the cavity
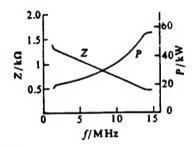

Fig.2 Electric field in a accelerating gap

Fig.3 Shut impedance Z and power
dissipation P *vs* frequency
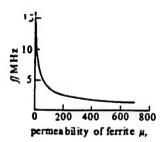
Fig.4 Dependance of frequency
on pereability of ferrite
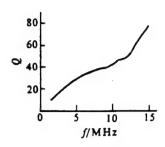
Fig.5 Dependance of merit factor
on frequency

TABLE 1. Main Parameters of Acceleration System

Table 1 Main parameters of accelerating system

Frequency/MHz	1.4～14.0	Ferrite ring dimensions/mm	500×320×25
Peak RF voltage/kV	7.2	Number of ferrite rings	2×25
Peak RF power/kW	60	Bias current/A	5～1500
Ferrite material	TDK–SY6	Number of Bias turns	4

From the curves of the cavity power dissipation versus
frequency as shown in Fig. 3, when the frequency is 14.8MHz, the
power dissipation of the cavity will be 55.9kW. Since the power
dissipation of the beam current is very small, a 60kW-RF
transmitter can well meet the requirement. From Fig. 4, when the
TDK-SY6 magnetic conductivity of the loaded ferrite material μ_r
changes from 700 to 2, the frequency will change from 1.4MHz to
14.8MHz, while the bias current changes in the range 20-6000A[6].
Yet this range can be reduced to 5-1500A if four turns of bias
coils are employed. A total of 2x25 ferrite rings is applied in
the entire cavity so as to ensure that the acceleration voltage
can reach 7.2kV. The length of the cavity is 2.55m; in the
overall design of CSR, the line nodal length for placing the RF
cavity is 5.6m[7], which provides sufficient space for placing
the designed RF cavity. The main parameters of the acceleration

system derived from the foregoing calculations are listed in Table 1.

Through a SUPERFISH program, the two-dimensional electromagnetic field was calculated using the finite-element method. As a result, the RF parameters of the design cavity were obtained, in close agreement with the RF parameters derived from transmission-line theoretical calculations. In addition, the dependence of the acceleration electric field distribution and RF frequency on the magnetic permeability of ferrite material was also acquired. All these finding indicate that the results of this method prove to be more accurate[8].

REFERENCES

1 Gradner ISK. Ferrite Dominated Cavities. *CAS*, 1992.3
2 徐建铭. 加速器原理. 北京: 科学出版社, 1981
3 Lombardini PP, Schwartz RR, Doviak RJ. *Moore Scholl Report*, 1957, (58):5
4 Griff JE, Nicholls G. *IEEE Trans*, 1979, NS 26(3)
5 Halbach K et al. SUPERFISH–A Computer Program for Evaluation of Cavities with Cylindrical Symmetry. *Part Accel*, 1979, 7
6 Itano A and Takanaka M. RF Acceleration Cavity for TARN II. Proceeding for the 5th Symposium on Accelerator Science and Technology. Tsukuba, Japan, 1984
7 魏宝文等. 兰州重离子加速器冷却储存环. 兰州: 兰州大学出版社, 1994
8 Pagani C. Cyclotron Cavities. *CAS*, 1992.3

TWO RADIATING SYSTEMS WITH A BEAM
WAVEGUIDE OR VACUUM FLEXIBLE
ELLIPTICAL WAVEGUIDE FOR HIGH POWER
MICROWAVE APPLICATIONS

Zhong Zhefu and Liu Shenggang

Institute of High Energy Electronics
University of Electronic Science and
Technology of China
Chengdu, 610054

ABSTRACT: Two radiating systems for generating a
scanning high power microwave beam are presented.
The first one uses a beam waveguide to feed an offset
paraboloid antenna, which is suited as the overmode-
input waveguide. The second consists of an offset
paraboloid antenna fed by a multimode horn that is
linked to a vacuum flexible elliptical waveguide as
a method of limited elevation scan, which is simple
and suitable for a transmitter with single mode output
waveguide. Techniques of physical-optical analysis
were used to investigate the foregoing antennas. The
numerical results show that the gains and spillover
efficiencies are reasonable.
KEY WORDS: high power microwave, beam waveguide, vacuum
flexible elliptical waveguide, offset paraboloid,
duplexing grid.

O. Introduction

The field of high power microwave (HPM) refers to
electromagnetic waves with frequency in the 1-300GHz and pulse
power over 100MW. In fact, some components, with which the high
power microwaves can be produced, have been successfully
experimented with one after another, including relativistic
velocity modulated tube, relativistic magnetrons, relativistic
backward-wave tubes, multi-wave Cerenkov devices, virtual cathode
devices, and so on. Their maximum single pulse output power can
reach 15GW[1,2].

The common features of these high power microwave devices
lie in the application of electromagnetic oscillations generated
from the interaction between the relativistic electronic beam and
electromagnetic waves; the output pulse width values are in the
dozens of ns to 1µm, and a pulse repetition frequency in the
hundreds of hertz at a single time. As a whole, high power
microwaves have broad applications in fields such as space
technology, environmental protection, scientific research,
military industry, etc.

Two high power microwave transmission configurations are
proposed in this paper: one is a beam waveguide-fed offset
paraboloid antenna, which is applicable as an overmode-output
waveguide wave source. This system can be used to perform omni-
bearing wave beam scanning. The other is a vacuum flexible
elliptical waveguide transmission and offset paraboloid antenna
which is suitable as a single-mode output waveguide wave source.
Typically, this structure can be used to achieve 360^0 in azimuth,
60^0 pitch angle in scanning.

A physical-optical numerical analysis was done with these
two configurations. The results show that in the S-band, in the
first configuration prior to optimization (only spillover loss is

counted), the efficiency is 86.6%; gain 40dB; maximum scale 8m; the calibre of main reflector 4.83m, while in the second configuration, the efficiency is 96.7%; gain 42.5dB; caliber 5.05m; and this antenna can be carried by a vehicle. The offset paraboloid antenna can overcome some defects due to shielding of the feed source or secondary reflector, such as low efficiency, high side lobe level and larger standing wave. Hence, both configurations can realize tracking and share a common antenna for high power transmission using the duplexing grid. They can also be used to get rid of the undesirable effect of the higher orthogonal polarization component generated from the offset paraboloid on tracking accuracy.

1. Offset Paraboloid Antenna System Fed By Beam Waveguide Transmission
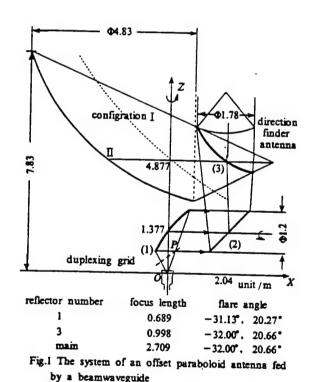
Theoretically, most of the GW level high power microwave (HPM) sources employ vacuum overmode output waveguides. In particular, in the short centimeter waveband, the application of beam waveguide transmission can serve as a convenient means for antenna scanning.

To avoid breakdown, the feed horn is designed to be quite open without allowing a refocusing process. With this offset paraboloid antenna, the shielding effect generated from the central feed mode can be avoided so as to get rid of the shielding loss and reflection as well as to reduce the standing wave ratio of the system, and to increase the power capacity together with decreasing the side lobe. This system is shown in Fig. 1, in which, two rotary axes provided by the beam waveguide enable the antenna to perform omni-bearing scanning (the designed and calculated wavelength is 10cm). In this figure, the imaginary line is configuration I showing only the main lens, and the solid line is configuration II.

The square pyramid multimode horn feed source applied allows an access to the radiation distribution of axial symmetry so that the spillover efficiency in the entire system can be improved. Its horn face field is

$$E_y = E_0 \sin \frac{\pi x}{a} (1 - 0.66 \cos \frac{2\pi}{a} y) \qquad (1)$$

where a is square pyramid mouth face side length. Technically, the square pyramid allows a stable polarization of the output line, which makes it easier to employ the duplexing grid to proceed with tracking. The output power is IGW; when a=30cm, the maximum mouth face field intensity of the multimode feed source is 38.2kV/cm.

reflector number	focus length	flare angle
1	0.689	−31.13°, 20.27°
3	0.998	−32.00°, 20.66°
main	2.709	−32.00°, 20.66°

Fig.1 The system of an offset paraboloid antenna fed by a beamwaveguide

Since there have been no systematic research results in the literature to date about the air breakdown intensity under

conditions of narrow pulse and low repetition frequency, we hereby can only refer to some references containing experimental results[2-4] and select point P, with a=30cm, input 1GW, on the axis below the first reflector as shown in Fig. 1; 0.7m from the horn face; field intensity 26.4kV/cm. If SF_6+N_2 gas is present between this point and the horn, and if the field intensity on one side of the air increases by a factor of 2, 52.8kV/cm, then the corresponding power input is 4GW.

To enhance the spillover efficiency, the ratio between the caliber of individual reflectors of the beam waveguide D and the wavelength is required to be larger than 10, and the distance between them should be $\ll 2D^2/\lambda$ so that they are located in the near regions. Then the entire system is analyzed through solving Eqs. (2)-(4) numerically using the physical-optics method.

$$E = \frac{1}{4\pi} \iint_s \{J_m \times \nabla - j\omega\mu J_e - j\frac{1}{\omega\varepsilon} [J_e \cdot \nabla]\nabla\}\Psi ds \qquad (2)$$

$$H = \frac{1}{4\pi} \iint_s \{-J_e \times \nabla - j\omega\varepsilon J_m - j\frac{1}{\omega\mu} [J_m \cdot \nabla]\nabla\}\Psi ds \qquad (3)$$

$$P = \iint_s (E \times H) \cdot n \, ds \qquad (4)$$

where, the free-space Green's function is $\Psi = e^{-jkr}/r$; the density of magnetic current is $J_m = E \times n$; the density of electric current is $J_e = n \times H$, and at the metallic reflector, $J_m = 0$, $J_e = 2n \times H$, where n is the line vector normal to the integration surface unit.

First, the E, H, spillover power P and surface electric current J_e at the first reflector are, respectively, calculated from the horn-face field. Then, the E, H, P and J_e at the second reflector are respectively calculated from J_e. This procedure is repeated until the far-field radiation characteristics (PO/PO) have been finally derived. Two configurations are calculated, from which the axis of radiation field and the rotary axis of azimuth in configuration I share a common axial line; while in

configuration II, 3, 4 of configuration I and main reflector are
moved 1.38m to the left so as to enhance the spillover
efficiency.   The calculations can be seen in Table 2.

TABLE 1. Spillover efficiency

reflector number	spillover efficiency(%)	
	I	II
1#	95.7	95.7
2#	92.96	95.83
3#	94.59	96.34
main reflector	98.02	98.05
overall	82.48	86.63

TABLE 2. Far-field Radiation Characteristics of
the Fig. 1 System

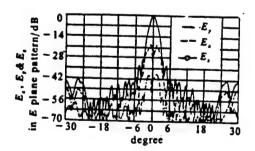| configuration	gain/dB	aperture efficiency/%	main lobe width	power flow density at 10km, I/W·cm^{-2}
I	40.686	50.86	1.5	0.815
II	40.436	48.02	1.6	0.808

Fig.2 The far field pattern of the configuration II

When the feed source becomes static, and the antenna
performs azimuth scanning, the polarization direction of the
radiation field will change.   In this case, the polarization

parallel to the symmetric plane of the offset paraboloid antenna will be defined as longitudinal polarization, and accordingly, the polarization perpendicular to the symmetric plane will be defined as transverse polarization. In fact, the gain of the transverse polarization is close to that of longitudinal polarization as shown in Table 3. The following calculation was done with transverse polarization. The far-field radiation characteristics in these two configurations are seen in Table 3.

Fig. 2 shows the far-field pattern of the configuration II, in which the orthogonal polarization component in the plane E is -19dB. There are two reasons for the low mouth-face efficiency: first, the edge taper of the beam waveguide is designed to be over -16dB with the expectation of increasing the spillover efficiency; second, the phase distribution of the mouth face is nonuniform.

The calculations suggest that the field has already offset the equiphase plane at the reflector. Thus, to improve the mouth-face efficiency, the plane mirror needs to be corrected so that the field can be an equiphase plane at the entry of the third reflector, and then the third reflector can be corrected so that the main reflector field can be close to a spherical wave centered with the focal point, and the field distribution can be made more uniform.

This configuration of beam waveguide feed allows the high field area in the lower half of the first reflector to be located in the upper half of the main reflector. This design can partially compensate for the field compression caused by the lower half of the 90^0 offset paraboloid and make the far-field pattern symmetric.

As for the scanning tracking practice of the antenna, it can be realized only by using another tracking radar since the HPM

repetition frequency is over low. However, if the tracking radar antenna is independent of the HPM antenna, then the follow-up calibration will become more difficult.

To solve this problem, one solution is to use the duplexing grid so that two radars can share the same antenna. Although the orthogonal polarization component of the 90^0 offset paraboloid is a bit large, the duplexing grid has the capability of filtering this component. Regrettably, the duplexing grid has its disadvantage, that is it will inevitably bring in certain losses.

The other approach is to install the antenna of the present tracking radar at the back of the third reflector. Since the field spot diameter of 1.6^0 HPM main lobes 279m at 10km, the distance 3.42m between the tracking radar axal line and HPM main lobe axis will not exert any significant effect on the tracking accuracy (it can also be compensated through the follow-up system). To prevent HPM from harming our own people and electronic systems, the beam waveguide is required to be placed inside a shielding cylinder, and both theory and experiment prove that the sufficiently large size of the cylinder (OD1.4m) will not yield any obvious effect on the field inside[5].

2. Offset Paraboloid Antenna System Fed By Flexible
   Elliptical Waveguide Transmission

At present, the S-band 1-GW relativistic magnetron which is now under development is based on the vacuum single-mode output waveguide. When the standing-wave ratio of the transmission and emission system is 1.5, the maximum field intensity inside the tube is 358kV/cm. Under vacuum conditions, narrow pulse and low repetition frequency are allowed. Hence, the smooth wall vacuum flexible elliptical waveguide transmission can be applied to achieve pitch angle scanning; its structure is in Fig. 3.

The $H_{10}^{\square}$ (or the H_{11}° of the circular waveguide) of the rectangular input waveguide is converted, through a rectangular (circular)/elliptical mode transformer, to an even H-wave EH_{11}, which is then converted, through an elliptical/square mode transformer via a 3-meter-long vacuum flexible elliptical waveguide to $H_{10}^{\square}$, and again is fed to the 90^0 offset paraboloid antenna through the multimode pyramid horn for 360^0 azimuth scanning.

The ordinary flexible elliptical waveguide is usually applied under aeration conditions. If a vacuum rubber sleeve (or bellows sleeve) is added at its outer sleeve, it can also be used under vacuum condition. If the plane E is bent, for instance, it is bent 10^0 every 1m, then it can be bent 30^0 for 3m, which can provide a 60^0 pitch scanning angle and attenuation 0.033dB/m, then it can be attenuated 0.1dB through the flexible elliptical waveguide.
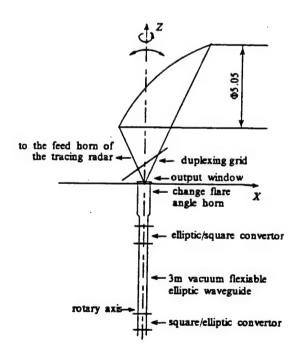
Fig.3 The radiating system with a vacuum
flexiable elliptical waveguide
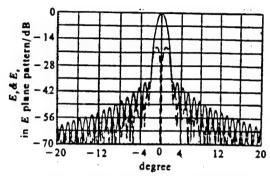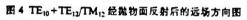
Fig. 4 The far pattern of the antenna fed
by $TE_{10} + TE_{12}/TM_{12}$

图 4 $TE_{10} + TE_{12}/TM_{12}$ 经抛物面反射后的远场方向图
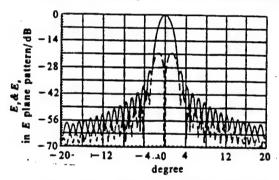
Fig. 5 The far pattern of the antenn fed by TE_{10}

TABLE 3. Far-field Radiation Characteristics of the Fig. 3 System

mode	spillover efficiency	aperture efficiency	gain/dB		main lobe width	
			transverse polarization	longitudinal polarization	E plane	H plane
$TE_{10} + \dfrac{TE_{12}}{TM_{12}}$	96.7	70.65	42.508	42.512	1.36°	1.36°
TE_{10}	88.6	53.59	41.365	41.123	1.82°	1.30°

43

With a semi-flare angle of the paraboloid selected as 25^0, the far-field pattern can be calculated under the multimode $TE_{10}+(TE_{12}/TM_{12})$ and single mode TE_{10} (see Figs. 4 and 5); the radiation indictor is shown in Table 3.

The losses of mode transformer and feed source horn are estimated to be 0.1dB. The feed source output of the tracking radar is sent to, through the duplexing grid set above the HPM horn, the paraboloid antenna. Normally, the tracking radar is in a temporary OFF state when HPM is in operation.

3. DISCUSSION

The major bottleneck in designing the high power microwave transmission antenna lies in how to prevent air breakdown and how to control the wave beam. The wave beamguide transmission configurations are applicable for relativistic magnetron and relativistic backward-wave tube with $TE_{10}^{\square}$ mode for the overmode waveguide output. For a relativistic backward wave tube with TM_{01}^0 output, the radiation mode transformer, such as a Vlasov-mode transformer or a quasi-anisotropic lens, can be used to convert TE_{01}^0 to linearly polarized quasi-Gaussian wave beams, and then, through the waveguide feed, wave beam scanning can be achieved.

During our design of the beam waveguide, we first focused on obtaining a high spillover efficiency and consequently, the edge taper was made greater than -16dB, which resulted in low reflection mouth-face efficiency. This fault, in fact, can be overcome through the shape design over different reflectors. This work is underway.

With the application of the duplexing grid, not only can the high power microwave transmission radar and tracking radar the same antenna, but also the undesirable effect of the greater

44

orthogonal polarization component resulting from the offset paraboloid antenna on tracking accuracy can be eliminated because of the duplexing grid's capability of filtering out the harmful polarization components.

From the analysis of the high power microwave experimental data available, the microwave air breakdown value with low repetition frequency and pulse width in the dozens to hundreds of nanoseconds is higher, by a factor of 2 to 3, than the known air breakdown in the continuous wave state. Even so, this topic still needs systematic and in-depth theoretical and experimental research.

REFERENCES

1 刘盛纲主编. 电子科技发展战略评析. 成都: 电子科技大学出版社, 1994
2 Benford J and Swegle J. High Power Microwaves. Arteh House, 1992
3 Treado T A and Doggett W O. *IEEE Trans*, 1988, PS16: 237−247
4 Lee T G and Konrad G T. *IEEE Trans*, 1985, PS13: 545−552
5 Cha A G and Imbriale W A. *IEEE Trans*, 1992, AP40: 1041−1046

1.5GHz CHINESE NIOBIUM SUPERCONDUCTING CAVITY:
PROGRESS IN RESEARCH

Wang Lifang, Zhang Baocheng,
Yu Jin, Wang Tong, Wu Genfa,
Geng Rongli, and Zhao Kui

Institute of Heavy Ion Physics
Peking University
Beijing 100871, China

ABSTRACT: Progress in research on the superconducting
cavity based on Chinese-derived niobium is introduced
with emphasis on the qualitative improvement of
the niobium and the corresponding superconducting cavity.
The designing of the cavity geometry, analysis of the RF
property of the niobium as well as its machining quality
are described. Special procedures of the cavity fabricating
and its post-processing are specified. Experimentally, the
gradient of 10MV/m and the quality factor of 10^9 at 2.5K are
given.
KEY WORDS: superconducting cavity, residual resistance
ratio, qualitative improvement of niobium material, quality
factor, accelerating gradient.

0. Introduction

Superconducting accelerators constitute one of the most
urgent issues and leading-edge topics with reference to the
development of new accelerator technology on a global basis, and

also as a product of present-day high-tech development.

Since the superconducting accelerator can provide extremely high electrical efficiency, as well as high quality beam currents with low energy dissipation and low transmittance, high energy accelerators, and free-electron laser devices with superconducting cavities were developed in foreign countries one after the other. Similarly, the development of niobium superconducting cavities has great significance in rapidly advancing RF superconductivity technology, and in developing high level accelerators and free-electron laser devices in China.

In April 1994, the first domestic 1.5GHz niobium superconducting cavity was successfully developed at the Institute of Heavy Ion Physics, Beijing University. In fact, until the present, only a few firms or laboratories in countries like Germany, the United States, and Japan are capable of developing or manufacturing niobium superconducting cavities.

The manufacturing of superconducting cavities not only is related to accelerator physics and its technology, but also involves some leading-edge subjects of metallurgy and material science. During the developmental process, we solved the major problem of deriving a superconducting cavity with high residual resistance ratio (ξ_R); after post-processing, the ξ_R value of the cavity was improved from 50-60 to approximately 300. At the same time, by mastering the machining quality of the niobium material, we smoothly carried out punch-shaping, fine processing, and electronic beam welding of the cavity. A cryogenic experiment demonstrated that the RF property of the improved niobium cavity was considerably upgraded: the accelerating gradient exceeded 10MV/m and quality factor was 10^9 at 2.5K, on a par with the advanced international levels.

1. Shape Design of 1.5GHz Niobium Cavity

In the first place, we decided to develop an elliptic superconducting cavity based on foreign experience in optimizing superconducting cavity design. In the geometrical design of the cavity, the 1993 latest version Superfish programs were applied. The guidelines in cavity shape design included optimizing the entire shape of the cavity if only the frequency is ensured, e.g., decreasing as much as possible the surface peak electric field E_p, i.e., lowering the E_p/E_a value, and decreasing the surface peak magnetic field H_p, as well as increasing the coupling factor K and shunt impedance R under a given average acceleration gradient E_a.

Since the superconducting cavity has an extremely low loss-resistance, shunt impedance can be neglected in optimizing the cavity dimensions. Therefore, only change in the surface peak electric field, the surface peak magnetic field, and the coupling factor are to be taken into account in optimizing the cavity shape.

We optimized the elliptic cavity dimensions including equatorial diameter, the size of accelerating gap, the radius of curvature of the circular arc, and the diameter of the beam tube as shown in Table 1. The geometric dimensions of the 1.5GHz superconducting cavity were determined by optimizing the computer programs. Table 2 shows the calculations of the optimized cavity shape using the Superfish programs.

TABLE 1. Fundamental Method of Geometric Designing
of the Optimal Nb Cavity

	expectation of optimum	affection after increasing the beam aperture	affection after increasing the outer circle radius	importance of parameters
E_p/E_a	−	+	−	●●
$R/M\Omega \cdot m^{-1}$	+	−	−	○
$H_p/E_a(Gs/MV \cdot m^{-1})$	−	+	−	●
K	+	+	+	●

R is shunt resistance, *K* is coupling coefficient, +: increase, −: decrease

48

Table 2. Physical Parameters of the 1.5 GHz cavity

F_0	R/Q	G	H_p/E_a	E_p/E_a	K
1486.637MHz	102	286	41.0G/MV/m	2.1	1.8

F_0 is resonant frequency; G is geometry factor

Selecting a material with ideal RF superconductivity is the first consideration in developing a superconducting cavity. Judging from the present situation of RF superconductivity, pure niobium can be considered as the first option material. Highly pure niobium with high residual resistance ratio can be acquired commercially. Yet niobium has poor thermal conductivity, and in this case, the thin niobium sheet punch shaping technique proves to be the best approach for achieving desirable heat dissipation and its homogeneity in all directions.

On the other hand, the quality of welding has a most dire effect on the RF superconductivity of the cavity. The unique feature of electronic beam welding lies in the fact that it can operate in high vacuum conditions and can be used to melt the parent material deeply without requiring metallic fillers, welding material and protective gas. Hence, it has little effect on the inherent property of the material.

2. Study of Quality Improvement of Chinese Niobium Material

2.1. Residual Resistance Ratio

The criterion for evaluating the performance of a superconducting cavity is as follows: whether or not it can acquire a high acceleration gradient. The highest acceleration gradient that a superconducting cavity can obtain is directly proportional to ξ_R. Thus, the performance of a niobium cavity can be expressed by ξ_R.

The definition of the residual resistance ratio is the resistance of niobium material under a constant temperature and its resistance ratio at the low temperature 10K, which can be expressed as $\xi_R = R_{300}/R_{10}$. Niobium material with high ξ_R can only be developed using the repeated vacuum electron beam melting technique, in which the content of gap impurities, including C, O, H, and N should be strictly limited, because these impurities display very poor thermal conductivity. The impurity contents of Chinese Nb sheet are listed in Table 3. According to the calculation based on Eq. (1), the residual resistance ratio ξ_R in the Chinese niobium material is lower than 50, which, obviously, is caused by the higher impurity contents of C, O and N. The computational formula is as follows:

$$\frac{1}{\xi_R} = \frac{O_{ppm}}{K_O} + \frac{C_{ppm}}{K_C} + \frac{N_{ppm}}{K_N} + \cdots \cdots \qquad (1)$$

where $K_O = 5000$, $K_N = 3900$ and $K_C = 4100$. Through repeated measurement of ξ_R in niobium samples, it was found that the residual resistance ratio in Chinese niobium ξ_R is only approximately 50, which means that this value is lower, by a factor of 3-4, than the requirements and basically conforms to the expected value in Eq. (1).
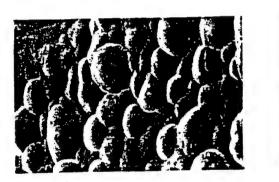
The major reasons for the foregoing situation are: the poor vacuum conditions in the electronic beam vacuum furnace; insufficient times of electronic beam melting; and improper temperature and improper post-processing period. In addition, electron microscopy showed that the grain size in Chinese niobium is inhomogeneous with spherical substances on its surface.
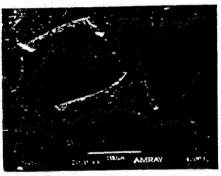
Fig. 1 shows a photograph of Chinese niobium before and after qualitative improvement. Based on the preliminary detection and cryogenic experimental results, we concluded that this niobium is not up to the quality requirements and therefore cannot be used to generate a high performance RF superconducting cavity. Whether or not the quality of Chinese niobium can be

50

improved emerged as a new problem, which was also a key to whether or not superconducting cavities could be made in China.

TABLE 3. Impurity Contents of Chinese Nb Sheet

Element	Si	W	Ti	V	Al	Fe	Mo	Zr	Hf	Cu	O	C	N	H
wt 10^{-6}	10	10	10	<10	<10	10	01	<10	<10	<10	20~50	30	40~50	<5

(a) no treated   (b)heat treated

Fig.1 The photograph of Chinese Nb before and after heat treated

2.2. Qualitative Improvement of Chinese Niobium Cavity

According to an agreement signed by Beijing University and American CEBAF, a joint research project on Chinese niobium cavity development was formed. Both sides agreed that the

qualitative improvement of Chinese niobium should be conducted using long-term heat treatment in ultra-high vacuum conditions. Three related experiments were completed successively, in which the working temperature was 1400^0C, the heat treatment period at high temperature was 4h, and the vacuum was 0.6μPa. The qualitative-improvement experiments were successful, through which the ξ_R value was improved from 61 to 470.

During the ultrahigh vacuum and high temperature niobium material treatment, with the rise in heating temperature in the vacuum furnace, the hydrogen atoms spread to the surface of niobium and recombined with Nb to form H_2, which escaped from the surface of niobium. Through heat treatment at upwards of 800^0C, the hydrogen content could be reduced to less than 10^{-6}. The oxygen combined with niobium and produced NbO and NbO_2 and then escaped. The diffusion of nitrogen in niobium was similar to the case of hydrogen, depending on the formation and evaporation of N_2. The carbon was evaporated from the surface of niobium by generating CO. This degassing mechanism is closely associated with the vacuum, heating temperature, and residence time in the vacuum furnace. The relationship between the concentrations of several gases and their partial pressure and temperature[2] is as follows:

$$C_O = 2.1 \times 10^{-4} P_{O_2} e^{\frac{60410}{T}}, \quad C_O = 1.48 \times 10^{-2} P_{H_2O} e^{\frac{45200}{T}} \tag{2}$$

$$C_H = 0.94 \sqrt{P_{N_2}} \, e^{\frac{23150}{T}}, \quad C_H = 0.38 \sqrt{P_{H_2}} \, e^{\frac{4200}{T}} \tag{3}$$

$$C_C = 1.07 \frac{P_{CO}}{C_O} e^{\frac{33600}{T}} \tag{4}$$

where P_{O2}, P_{N2}, P_{CO}, and P_{H2O} are the partial pressures with 1.33×10^2Pa as unit; C_N, C_O, C_H and C_C are the concentrations of the corresponding gases; $10^{-6}T$ is the thermodynamic temperature, K. From the foregoing equations, the partial pressure of individual gases in the ultrahigh vacuum furnace constantly decreased with an increase in the high temperature degassing time, resulting in

a decreased concentration of gaseous impurities.

To effectively remove the C, H, O, and N from the niobium
material, a proper gas-absorbing material must be used to
fabricate a protection layer. In our case, titanium was chosen
as this gas-absorbing material. Specifically, the 3x100x2.5
niobium sample was suspended in a thin titanium tube. Metallic
titanium melts at 1668^0C; pure titanium has a body-centered cubic
structure when it is above the phase-variation temperature; at
elevated temperatures, titanium is chemically active. When the
sample was heated at elevated temperatures in the $\leq 10^{-4}$Pa vacuum,
the titanium was evaporated to the surface of niobium and formed
a thin film dozens of μm in thickness, which could capture C, O,
H, and N in trace amounts. Later, through chemical treatment,
this film along with impurities could be removed.

In addition, during heat treatment, the impurity atoms in
the vacuum furnace were absorbed by titanium so that niobium
could be prevented from becoming repolluted. Through ultrahigh
vacuum (better than 10^{-4}Pa) and high temperature (over 1250^0C)
treatment in this furnace with titanium protection, the content
of various gases could be decreased to the 10^{-6} order of
magnitude, and the ξ_R in niobium material can possibly reach
values in the hundreds or even nearly a thousand.

The treatment test of niobium samples was accomplished,
respectively, at the Beijing Non-ferrous Metal Research Academy
and Beijing Iron and Steel Research Academy. The ξ_R value in the
improved niobium material reached 264 in the test conducted in
Beijing Iron and Steel Research Academy. Table 4 lists the
results of heat-treating Chinese niobium samples, derived in
different laboratories.

From the photograph of Nb samples after qualitative
improvement as shown in Fig. 1(b), the grain size in niobium

became larger and homogeneous, and the spheroidal substances disappeared. With reference to the measurements of ξ_R, the Rf superconducting property of niobium was remarkably improved. Fig. 2 is the thermal conductivity curve and the corresponding ξ_R curve of the Chinese niobium samples before and after qualitative improvement.

TABLE 4. Results of Heat Treating Chinese Nb

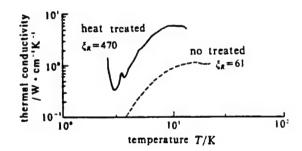| Heat processing facilities	Vacuum pressure in the furnace /Pa	Temperature of heat processing /°C	Time /h	protecting material	ζ_R
NINMR(Baoji)	10^{-3}	1100	1.5	Y	37~40
CEBAF(USA)	10^{-7}	1400	4	Ti	470
KEK(Japan)	10^{-4}	1250	6	Ti	232
BINMR(Beijing)	10^{-3}	1050	4.5	Ti	40~59
BIFMR(Beijing)	10^{-3}	1400	4	Ti	264

Fig.2 The thremal conductivity curve and ζ_R value of Chinese Nb and heat treated

Following a large number of qualitative improvement tests on niobium sheet samples, the post-processing technology for the Chinese niobium cavity was determined. Its basic indicators included: processing temperature 1250^0C-1400^0C; vacuum condition better than $10^{-4}Pa$; heat treatment period 4-6h, and titanium or yttrium protection layer. Hence, the qualitative improvement processing of Chinese niobium cavity was successfully realized.

3. Shaping of 1.5GHz Chinese Niobium Cavity

To master the punch shaping and machining technology for niobium sheets, tests were carried out on the performance of Chinese niobium material. Through a comparison of test results, it was found that the performance of highly pure copper sheet is similar to the performance of niobium sheet. To avoid thermal instability that may occur due to the defects generated in the development of the niobium cavity, we decided to first conduct copper cavity pre-processing before processing the niobium cavity.

In fabricating punch dies, we had several considerations as follows: (1) the die material should not lead to surface smearing of the niobium sheet; also, it should have adequate hardness but should not scratch the surface of the sheet; (2) the punching steps should be arranged properly so that punching will not cause any wrinkle or thickness nonuniformity of the material; the depressuring pieces should be easy to demold, and (3) the processing stock of electronic beam welding should be ensured.

Based on the foregoing requirements, we designed punch dies for the 1.5GHz niobium cavity. Fig. 3 is a photograph showing this die set. As a matter of fact, with this die set, the punch-shaped niobium cavity did not show any wrinkles or scratches and retained the original surface fineness. During punching, the dies, pressing machine, and surroundings were kept clean so that no external impurities could incise the niobium surface.

The quality of electronic beam welding strongly affects on the superconductivity of the niobium cavity. Therefore, welding procedures are required to be in strict coordination; also, the defocusing welding technique and appropriate welding technological parameters are required, as well.

Prior to welding the niobium cavity, we conducted numerous welding tests on niobium sample sheets. Owing to the careful preparations and reliable test data, the entity welding of the niobium cavity was a success. Fig. 4 shows the 1.5GHz Chinese niobium cavity.
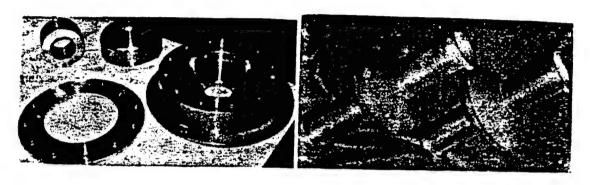
4. Results of Cryogenic Superconductivity Experiment

A two-step cryogenic superconductivity experiment was accomplished for the Chinese niobium cavity. The first-step experiment was arranged before the high temperature qualitative improvement test, i.e., the ξ_R value was only approximately 50. Through the cryogenic experiment, the quality factor of the cavity Q was measured as only 3×10^8, the acceleration gradient was 4.5MV/m. The test result indicated that the performance of the niobium cavity basically conformed to the theoretical expectations, while a superconducting cavity with a lower ξ_R value could not provide a high acceleration gradient.

In October 1994, qualitative improvement and post-processing were made for the niobium cavity, and a more intensive experiment was carried out in November of the same year. Under the temperature 2.5K, the quality factor of the cavity Q was measured

as 10^9, and the acceleration gradient was higher than 10MV/m suggesting that due to the successful qualitative improvement, a higher residual resistance ratio ξ_R was derived, and a Chinese niobium superconducting cavity with an ideal RF superconductive property was successfully developed.

REFERENCES

1   Padamsee N. The Technology of Nb Production and Purification. Presented at the workshop on RF Superconductivity. CERN, Geneva July 1984

2   Kneisel P. Some Preliminary Results on the Degassing of Niobium with Titanium. SRF. July 1984

THERMAL DISTORTION AND DAMAGE OF OPTICAL COMPONENTS SUBJECTED TO CONTINUOUS-WAVE (CW) DF HIGH POWER LASER IRRADIATION

Xiong Shengming and Zhang Yundong

Institute of Optics and Electronics
China Academy of Science,
P.O. Box 350
Shuangliu, Chengdu 610209

ABSTRACT: The absorption distributions for quarter-wavelength coating stacks and enhanced metal-dielectric reflective coatings are analyzed in this paper. The thermal distortions of optical components subjected to CW DF high power laser irradiation are computed and measured. The calculated data is compared with experimental results.

KEY WORDS: thermal distortion, laser damage, multilayer coating, DF laser.

0. Introduction

A continuous-wave laser differs from a pulsed laser, and likewise does the damage mechanism of the optical components in these two laser systems.

Typically, a pulsed laser operates in an extremely short period of time, during which the electric field exerts a predominant effect only on the first several coatings of the

multilayer coated optical components, and serves as the major cause of damage to the optical components. In contrast, a continuous-wave laser operates in a longer period of time, during which the damage is largely subject to a thermal effect. Generally, when a beam travels within time period of a picosecond and nanosecond order of magnitude, the effect of the electric field predominates. Yet when the beam travels in time period of the microsecond order of magnitude, the thermal effect becomes critical for the optical components.

Normally, a high power continuous-wave laser system is composed of a non-cooling ultra low expansion vitreum (ULE), microcrystalline vitreum (CER-VIT), fused quartz, BK7 vitreum, as well as reflective optical components such as cooling copper, molybdenum, silicon, and so on.

Technically, the polished substrates will be coated with a metallic coating, which, again, will be coated with multilayer coatings to make a specified laser wavelength reach maximum reflectivity. In some optical components, however, to enhance the laser damage threshold, the substrates will be coated with multilayer reflective coatings with very low absorbance, and different high and low refractivities.

The optical components with multilayer coatings can be subjected to thermal deformation under high power laser irradiation because of the absorption of the material itself and the absorption introduced during coating process. If the absorption is overly large, it can even damage the coating and the optical component. In a laser transmission system, thermal distortion of optical components can lead to the distortion of optical images, and to the distortion of laser wave surface, which can affect laser beam transmission. Therefore, it is of high practical interest to study the thermal distortion and

damage of reflection optical components under high power laser irradiation.

1. Instantaneous Temperature Distribution in Multilayer Coatings under High Power Laser Irradiation

Generally speaking, due to the coating material and coating process, multilayer coatings are subject to absorption and scattering, which can take place either inside the coating or at the interface between coatings or between the coating and the substrate.

It is found from the experiments that the absorption mainly occurs at the interface between coatings and between the coating and the substrate[1]. The absorption of multilayer coatings can not only restrict the reflectivity and transmittance of optical components, but more importantly, can result in thermal distortion and damage of optical components in a high power laser system. The temperature rise in multilayer coating stacks and optical components, caused by high power laser irradiation, can be computed based on the theory given in reference [4]. By referring to references [2, 3], the absorption distribution at the interface between coatings can be derived as follows:

$$A_i = \left\{ \left[1 - R - \frac{4n_s^+}{n_H^2} \left(\frac{n_L}{n_H} \right)^{2N} \right] - \left[\frac{4\pi\sigma (1.15 - 2.565 \times 10^{-6}(50 \times 10^3 - \lambda))^{2N}}{\lambda} \right]^2 \right\} \cdot$$

$$\cdot \left\{ \left(n_H^2 - n_L^2 \right)^{-1} \left[1 - \left(\frac{n_L}{n_H} \right)^{2N+1} \right] \times 4 \right\}^{-1} - \frac{\lambda}{8} (\beta_L - \beta_H) \tag{1}$$

2. Thermal Distortion of Optical Components and Its Measurements

Typically, under high power laser irradiation, the optical components can be heated and yield to thermal distortion as the coatings and substrates absorb laser energy. Furthermore, if

they absorb too much laser energy or if the absorbance of optical components is excessive, then the optical components may suffer from damage under high power laser irradiation.

In fact, many factors can cause the thermal distortion and damage of optical components. For instance, in two kinds of reflection mirrors commonly used in high power laser systems, i.e., cooled mirror and noncooled mirror, their damage mechanism and thermal distortion under laser irradiation are different. This paper discusses the noncooled mirror.

Usually, if the noncooled mirror used in a high power laser system is required to bear a high power density, ULE, CER-VIT, fused quartz, silicon and molybdenum are usual options for the substrate material. But if the noncooled mirror only deals with a low power density, BK7 vitreum can be chosen as the substrate material. Typically, when the entire or part of an optical component is uniformly irradiated by a laser beam, the coatings and substrates will absorb laser energy and generate a temperature gradient inside. This temperature gradient can bend the optical component with a bending spherical radius as follows [5]:

$$R_s = t / [\alpha_1 (\Delta T_s^F - \Delta T_s^B)]$$

(2)

where α_1 is the thermal expansion coefficient of the substrate; t is the thickness of the substrate. To bend the substrate plate into a curvature with a radius R_s, the following load is needed:

$$Q_0 = 8D(1 + \mu_0)/(R_s^2 - R^2)$$

(3)

If the optical component is supported by a circular perimeter, then the central offset (thermal distortion) is

$$\Delta_0 = 0.01563 Q_0 R^4 / D + 0.0625 Q_0 R^4 / [D(1 + \mu_0)]$$

(4)

where R is radius of optical component; μ_0 is Poisson's ratio of the substrate, $D = Et^3 / [12(1 - \mu_0^2)]$; and E is Young's modulus. Again, if the circular optical component is supported by three

points separated with an angle of 120^0, then the central offset
is

$$\Delta_0 = 0.0362 Q_0 R^4 / D \tag{5}$$

The foregoing analyzes the causes of thermal distortion of
optical components under laser irradiation. Whether or not this
analysis is logical must be verified through by making
measurements.

In fact, thermal distortion and damage that occurred in a
series of different substrates and different coating structures
under high power DF laser irradiation were tested. The test
setup is shown in Fig 1. The thermal deformation and thermal
diffusion of the mirror was tested using a Twyman-Green
interferometer; the interference fringes were input into a
computer through a CCD video camera for sampling and logging, and
then they were outputted into a television monitor to be observed
and adjusted. Technically, the computer was able to collect 16
frames of interference images per second.

The DF laser in the experiment was a kilowatt level non-
stable cavity laser developed at the Handan 718 Research
Institute. The DF laser beam emitted from a laser device was
split into two beams while passing through an optical wedge.
Most of the transmitted DF laser beam was reflected from a copper
mirror, and the reflected laser beam was focused through a single
CaF_2 lens with focal length f=1m. In this case, the DF laser
beam diameter at the test mirror was approximately 1mm.

To maintain the reflectivity of the 3.8μm wavelength
invariant, the incident angle of the DF laser beam at the test
mirror was set to be smaller than 25^0.

When the test mirror was irradiated by the high power
density DF laser, a temperature gradient was formed in the

63

coating system of the test mirror due to the absorption and
scattering by the coatings and substrates. As a result, the test
mirror was subject to local thermal deformation. As seen in the
interferometry diagram, the thermal deformation caused the
interference fringes to change. Therefore, based on the
dimension and range of the change of interference fringes, the
dimension and range of the thermal deformation can be accordingly
determined. Eventually, through thermal deformation, the
temperature gradient and laser damage of the optical component
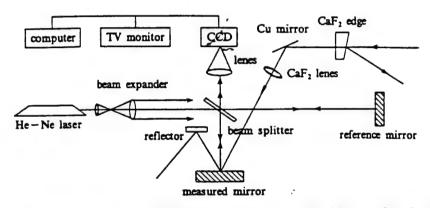under laser irradiation can be derived.

Fig.1 The measured setup of the reflector thermal distortion under high power laser irradiated

3. Theoretical Calculations versus Test Results

In the experiment with the thermal deformation of the laser
reflection mirror, a non-stable cavity DF chemical laser device
was used. The DF laser power fluctuated between 200-400W, with
light spots shaped in circular rings, and the internal and
external diameter, respectively, were OD30 and OD20mm. At the
test mirror, the laser beam was focused into a light spot with a
dimension of OD1mm. With the transit time τ as 1s, the DF laser
output power was different during each measurement. Fig. 1
indicates the diffusion range of thermal distortion of the
optical component under different substrates, different coating
systems, as well as different DF laser power. Fig. 2 shows an
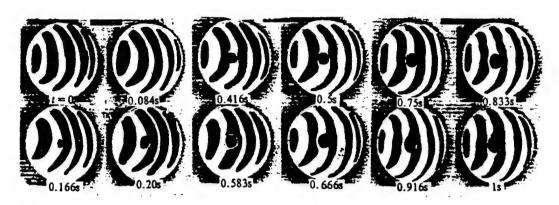interferometry diagram of thermal distortion.

64

Fig.2 Interferometry diagram of thermal distortion for the reflector with coating $G/(H_1L')^6H_1/Air$

For the all-medium coating system $G/(H_1L')^6H_1/Air$, a theoretical calculation was made on the thermal distortion range and central thermal distortion of the enhanced metallic coating system $G/Ag(L'H_1)^2/Air$ under DF laser irradiation. Fig. 2 indicates the thermodynamic properties of various substrates[5]. At the wavelength of the laser beam, the refractivity(IAD) of ZnS, BaF_2+CaF_2 (1:1) is $n_{H1}=2.26$ and $n_{L'}=1.36$. The thermal diffusion and thermal conductivity of the Zns, BaF_2+CaF_2 mixed coating are: Zns: $\alpha_s=0.00813cm^2/s$, $k_s=15.66mW/cm \cdot C$; BaF_2+CaF_2: $\alpha_s=0.00853cm^2/s$, $k_s=11.17mW/cm \cdot C$.

Prior to calculating the thermal distortion of the coating system caused by DF laser irradiation, several assumptions were made, for instance, the adhesive pressure of the coating was assumed to be $P=10^5N/cm^2$; the surface roughness of the substrate was assumed to be $\sigma=3nm$; the substrate to be fused quartz vitreum, and DF laser travel time to be $\tau=1s$.

Given the following conditions: the same coating, three substrates, and different laser power density, the temperature rise and thermal deformation in front of the substrates are shown in Table 3.

65

TABLE 1. Thermal Distortions of Optical Components with Different Coatings and Substrates Under DF Laser Irradiation

substrate	coating	DF laser power/W	reflectance	distortion diffusion/mm
BK7	$G/(H_2L')^4H_2$/Air	200	0.99	10.6
ULE	$G/(H_1L')^4H_1$/Air	374.4	0.987	3.6
SiO_2	$G/(H_1L')^4H_1$/Air	237.2	0.987	10.6
BK7	$G/(H_1L')^4H_1$/Air	393.1	0.987	15.6
ULE	$G/Ag/Y_2O_3$/Air	370.2	0.985	10.6
BK7	$G/Ag(L'H_1)^1$/Air	200.0	0.989	15.0
SiO_2	$G/Ag(L'H_1)^2$/Air	200.0	0.994	9.8
BK7	$G/(H_1L')^4(H_1L)^4H_1$/Air	200.0	0.987	13.6
SiO_2	$G/Ag(L'H_1)^1$/Air	200.0	0.989	9.1
BK7	$G/Ag(L'H_1)^2$/Air	200.0	0.989	12.1
ULE	$G/Ag(L'H_1)^2$/Air	200.0	0.994	—
Si	$G/Ag(L'H_1)^2$/Air	200.0	0.994	—
Mo	$G/Ag(L'H_1)^2$/Air	200.0	0.994	—

Note: H_1为ZnS, L'为BaF_2+CaF_2, L 为TbF_3, H_2为ZnSe

TABLE 2. Thermodynamic Properties of Substrates

substrate	Young's modulus $E/N·cm^{-2}$	diffusivity $\alpha_s/cm^2·s^{-1}$	conductivity $k_s/W·(cm·℃)^{-1}$	expand coef. $\alpha/℃$	Poisson radio μ_0
Mo	2.172×10^{11}	0.529	0.145	4.96×10^{-6}	
SiO_2	7.3×10^{10}	8.25×10^{-3}	0.0014	5.6×10^{-7}	0.17
ULE	6.76×10^{10}	8.25×10^{-3}	0.0014	3.0×10^{-8}	0.247
BK7	3.16×10^{11}			8.3×10^{-6}	0.208

For the coating system $G/Ag(L'H_1)^2$/Air, the calculation results are similar to those for the all-medium reflective coating. As far as the interference measurement is concerned, this technique can be used to measure the variation of area image $\lambda/20$ of the entire mirror. During the experiment, the change of

the thermal deformation $\lambda/20$ was assumed to be reflected in the interferometry diagram, i.e., the 0.031μm thermal distortion could be detected. Based on this assumption, the range of the thermal distortion and its maximum change can be determined theoretically.

Fig. 4 shows a comparison between the calculations and experiment results of two coatings and three substrates, in which $_0\Delta$ is the maximum thermal deformation of the mirror surface under DF laser beam irradiation; Φ is the expansion due to thermal deformation.

TABLE 3. Calculated Distortion for Coating $G/(H_1L')^6H_1/Air$ and Different Substrates

distance departing from original/cm	temperature rise of face for substrate/℃			thermal distortion/μm		
$R_2 = R_1 = 0.05$	43.3^Δ	68.34^*	$69.9^\#$	0.503^Δ	0.046^*	$12.68^\#$
$R_2 = 0.2$	20.8^Δ	32.8^*	$33.5^\#$	0.256^Δ	0.0222^*	$6.088^\#$
$R_2 = 0.3$	4.68^Δ	7.38^*	$7.55^\#$	0.0578^Δ	0.005^*	$1.369^\#$
$R_2 = 0.5$	2.68^Δ	4.22^*	$4.41^\#$	0.033^Δ	0.003^*	$0.782^\#$
$R_2 = 1.0$	0.37^Δ			0.002^Δ		

Note: Δ: fused silica, $I_0 = 54\,kW \cdot cm^{-2}$, $\alpha_0 = 0.0095$; $*$: $I_0 = 845\,kW \cdot cm^{-2}$, ULE substrate;

$\#$: BK7 substrate, $I_0 = 86.5\,kW \cdot cm^{-2}$.

TABLE 4. Comparison of Calculated Thermal Distortion with Measurements

substrate	coating	DF laser power density /kW·cm^{-2}	central thermal distortion /μm	calculating data /mm	measuring results /mm
BK7	$G/(H_1L')^6H_1/Air$	94.68	12.68	18.0	15.9
ULE	$G/(H_1L')^6H_1/Air$	84.5	0.046	3.60	3.6
SiO$_2$	$G/(H_1L')^6H_1/Air$	53.5	0.535	10.0	10.6
BK7	$G/Ag(L'H_1)^2/Air$	45.1$^{*)}$	15.907	22.0	12.6
ULE	$G/Ag(L'H_1)^2/Air$	45.1	0.059	3.00	—
SiO$_2$	$G/Ag(L'H_1)^2/Air$	45.1	1.084	11.0	9.8

*) this date is inaccurate.

4. Conclusions

The theoretical analysis and actual measurements of the thermal distortion of the coatings indicate that:

(1) Under high power DF laser density irradiation, different substrates and different coating designed will absorb laser energy, and thermally deform optical components.

The extent of thermal deformation and the diffusion of thermal distortion of optical mirrors are different for the same coating material, and the same coating with different substrate materials. This is related to thermodynamic properties of the substrate materials. Substrate material with small thermal expansion and small thermal diffusion is subject to small thermal deformation. On the other hand, material with a large thermal expansion coefficient will undergo large thermal distortion. In fact, the largest thermal deformation takes place in the mirror with a BK7 substrate.

For the same substrate with different coatings, the thermal deformation value and the thermal diffusion range are different. This is associated with the absorption and scattering of the coatings in the coating system as well as their thermodynamic properties. Under 100kW level DF laser power density, the thermal deformation of the BK7 vitreum mirror with 3.8µm wavelength as the unit is 4.2λ, and the deformation is λ/3.5 for the fused quartz substrate, and λ/64 for the ULE substrate;

(2) For the all-medium coating system, the calculated thermal deformation is in agreement with the measured value, while for the metallic coating system, the calculated value is different from the measurements. This is probably because the reflectivity of the reflective coating and laser power density were not accurately measured. Another reason is that the calculation covered the substrates and the metallic coating as a

whole without considering the thermodynamic properties of the metallic coating.

(3) It was found from the experiment that in two kinds of substrates: fused quartz and ULE, the thermal deformation of the metallic coating is smaller than that of the all-medium reflective coating. This indicates that the substrate with metallic coating is better than the substrate with an all-medium coating, and the reflectivity of the former is higher than that of the latter.

(4) In the same substrate with all-medium reflective coating, the thermal deformation and damage of the mirror are different under materials with different high and low refractivities. It was also found from the experiment that the coating Zns with high refractivity is better than ZnSe, and the coating YbF_3 with low refractivity is superior to the BaF_2+CAF_2.

(5) For the same coating system, the substrates made of metal molybdenum and semi-conductor silicon show outstanding supremacy when applied in the continuous wave high power DF laser. And there is no thermal distortion occurring under 100kW level DF laser power density. This may result from the ideal thermal conduction and thermal diffusion performance of these two materials.

REFERENCES

1   Temple P A, Decker D L, Donovan T M and Bethke J W. Laser Induced Damage in Optical
    Materials. *NBS Special Pub*, 1978, 541:37~42
2   Bennett H E and Burge D K. *J Opt Soc Am*, 1980, 3:268~276
3   熊胜明. 中红外高功率激光薄膜[硕士论文]. 成都：中国科学院光电技术研究所，1992
4   Palmer J R. *SPIE*, 1986, 655:241~261
5   James R Palmer. *Optical Engineering*, 1983, 22(4):435~445

NUMERICAL SIMULATION OF HIGH VOLTAGE PULSED POWER CONDITIONING SYSTEMS

Yang Libing and Gao Shunshou

Institute of Fluid Physics
CAEP
Chengdu, Sichuan, 610003

ABSTRACT: Numerical simulations of high voltage pulsed power conditioning system (inductive stage/opening switches) are given in this paper. According the different initial energy, the capacitor model and simple MFCG model are computed. For the second model, two cases--not carrying opening switches load and carrying opening switches load are considered, the results show that the current will change 20%-30%. In the capacitor model, the effects of load, initial charging voltage, inductive storage et al. are considered. By using the numerical results for which only the running parameters in the system are optimized, some effective output results ar possible.

KEY WORDS: power conditioning system, electrical exploding opening switches, electrical resistivity, numerical simulations.

0. Introduction

At present, countries such as the United States, Britain,

71

and France are demonstrating their strong interest in developing pulsed power technology and are taking the initiative in fostering their corresponding research tasks.

Among other aspects, one pulsed power device is particularly interesting: this device is constructed of three integrated parts, namely, magnetic flux cumulation generator (MFCG), power conditioning system, and operational load.

Theoretically, the MFCG is an intensive pulsed power supply which can transform explosive anergy into magnetic anergy and can supply several hundreds of millions of joules of energy and hundreds of millions of amperes of pulsed electric current. Moreover, its energy density can reach up to $10^{11} J/m^3$, and its energy conversion efficiency is as high as over 10%.

Yet if the MFCG is used as an energy supply for plasma physics and electron beam physics experiments, its output pulse voltage is required to possess an extremely high amplitude (hundreds and   thousands of volts) and have a fairly steep leading edge. In addition, the MFCG generally serves as a low impedance anergy source which can be directly applied only in low impedance
($<m\Omega$) loads. Thus, in actual applications, only by combining MFCG with an appropriate power conditioning system can the ideal electric pulses with high amplitude, high power and steep leading edge be achieved and applied in different kinds of loading systems.

Normally, the key components in the power conditioning system include a high voltage transformer and opening switches. So far, there are mainly two kinds of electric circuit structures: transformer/opening switches and inductive storage /opening switches. Based on the current condition, we conducted a systematic study on the inductive storage pulsed power conditioning system with electrical exploding opening switches

(EEOS). The result showed that the electrical exploding opening
switches of this kind can generate a great resistance change
rate, from which, the maximum resistance can reach nearly a
hundred ohms, and voltage pulses with a leading edge
approximately 80ns and an amplitude over 600kV can be generated,
and the pulsed current passing through the opening switches can
reach up to dozens of kiloamperes.

1. The Process of EEOS

When the pulsed current passes through a metallic conductor,
it will heat the conductor (joule heating). With the rise in
temperature, the metallic conductor will be subjected to a series
of thermophysical processes, including melting and gasification;
accordingly, its resistivity will constantly increase.

Supposedly the conductor, during the gasification, comes
across a sudden short-circuit and breaks down to become a plasma
(electric arc), and then quickly expand to form an electric
explosion, its resistivity will grow hundreds of times. In this
case, EEOS will act as a high resistance short-circuit component
in the pulsed circuit. It is because of this abrupt increase in
resistivity that voltage pulses with a fairly high amplitude and
steep leading edge can be produced in the load.

As far as research on electric exploding foils is concerned,
a great deal of profound work was done at the Los Alamos National
Laboratory in the United States and some research institutes in
Russia. As a result, a more comprehensive database system and a
variety of simulation computing programs were developed. The
theoretical models established include a 2D electric explosion
static theoretical model [1,2] and an electric explosion
experimental model [3,4,5].

In the 2D electric explosion static theoretical model, the

resistance change in the metallic conductor is described with two fundamental processes, namely a fixed phase heating process and phase variation process. The resistivity change equations of the two stages can be determined through the law of conservation of energy[1].

The computational method developed by C. Maisonnior et al. aims at determining the cross-sectional area of the conductor through the action volume, and to determine parameters such as the conductor length in terms of the energy consumption. This experience proved to have a relatively high reference value in system engineering design. However, in terms of concrete simulation computations, the Azarkevich theoretical model seems more suitable for experiments.

In the Azarkevich theoretical model, the variation of resistivity ρ during metal heating, melting, gasification as well as explosion can be expressed with the product of two factors as follows:

$$\rho = \zeta \cdot \eta$$

(1)

where $\zeta = \zeta(w)$ is the function of specific energy w; $\eta = \eta(w,t)$ is related to the inertia of the explosion product; $\zeta(w)$ is the dashed-line formula expressing the relation

$$\zeta = \zeta_i + \beta_i (w - w_i) \quad (i = 1, 2, 3, 4)$$

(2)

where ζ_i and w_i are the break-point values; β_i is an angular coefficient. Point 1 corresponds to room temperature status; points 2 and 3, respectively, correspond to the origin and terminus of melting; point 4 corresponds to the binding energy of the metal. Here η is described from the following equation:

$$\begin{cases} \eta = 1 & w < w_s \\ \eta = \eta(w, t) & w \geq w_s \end{cases}$$

(3)

where w_s corresponds to the initial energy at the explosion stage; ζ_i, β_i, and w_i mainly depend on the materials employed.

74

2. Simulation Computation Result and Analysis

For the capacitor model, the equivalent electric circuit corresponding to the power conditioning system is shown in Fig. 1, where C is capacitor group; L_n is inductive storage; R_e is conductor resistance; C_{ob} is sharpening capacitor; R_f is load; K_1 and K_2 is separating gap switches.

The differential equations of the electric circuit are as follows:

$$L_n \frac{di_1}{dt} + i_e R_e = V_c \qquad (4)$$

$$\frac{dq}{dt} = -i_1 \qquad (5)$$

$$\frac{dq_{ob}}{dt} = i_c \qquad (6)$$

$$i_1 = i_e + i_c + i_R \qquad (7)$$
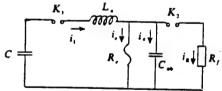
When t=0, $i_1 = i_e = i_c = i_R = 0$, $V_c(0) = V_0$ (the initial charged voltage of the capacitor C); when the separating gap switches K_2 reaches the breakdown voltage and gets connected, $i_R = i_c R_e / R_f$, and then by taking into account $q = CV_e$ and $\rho l / A$ (l is conductor length), and Eqs. (1)-(3), numerical calculation can be conducted for the circuit differential equations.
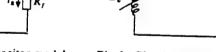

Fig.1 Circuit diagram of the capacitor model   Fig.2 Circuit diagram of the simple MFCG model

In the simple MFCG model, only a relatively simple axial detonation MFCG model [6] is considered. In this model, the metal sleeve is filled with explosives, and externally it is coiled, and the initial energy of the coil is supplied by the capacitor. Thus, the MFCG can be approximated to have an initial

75

electric current, an inductance coil with inductance L_G (equivalent to the MFCG) attenuated with time, its equivalent electric circuit being shown in Fig. 2.

Considering the design of the generator and its operational principle, and assuming that due to very small energy consumption in resistance loss and rapid operation of the generator, the magnetic field does not penetrate into the sleeve, then in this case, the differential equations corresponding to the electric circuit are as follows:

$$\frac{d}{dt}[L_G+L_a]i_1+i_1R=0 \qquad (8)$$

$$i_1=i_e+i_c+i_R \qquad (9)$$

$$i_c=\frac{dq_{ob}}{dt}$$

$$(10)$$

where $L_G=L[(1-r^2/r^2_2)]$, $r=r_1+v_b t$, $R=R_e+R_H$, $R_H=-K \cdot dL_G/dt$, $K(t)=\alpha t$. Here, L is the initial inductance equivalent to MFCG; r_1, r_2 are the sleeve and the radius of the equivalent coil; v_b is the speed of the explosive detonation; R_H is magnetic leakage factor which is described through a linear function $K(t)$ (K is non-dimensional).

However, in the forgoing equations, the effect of skin depth, skin resistance, as well as some distributive resistances are neglected. Similarly, when the initial condition t=0, $i_1(0)=i_0$, $i_e=i_c=i_R=0$, and after the separating gap switches K2 reach the breakdown voltage and is connected, $i_R=i_eR_e/R_f$, and then by taking into account $R_e=\rho l/A$ as well as Eqs. (1)-(3), can the differential equations of the circuit be given numerical solutions.

In the capacitor model, the effect of load, sharpening capacitor C_{ob}, initial charging voltage V_0, inductive storage L_R, and electric explosion cross-sectional area S on the voltage output at the upper end of the explosive wire, respectively, is

calculated as shown in Figs. 3 to 7.

A conclusion can be reached from Figs. 3 to 7, namely that when the loaded resistance increases from 15Ω to 40Ω, the voltage output at the upper end of the explosive conductor nearly doubles. Additionally, the sharpening capacitor C_{ob} affects the leading edge and amplitude of the voltage: the capacitor value increases, the voltage amplitude decreases, the voltage rise time increases, but the pulse width broadens somewhat. Hence, C_{ob} can play a role in sharpening the waveform in the electric circuit.

Among other things, the higher the initial charging voltage of the capacitor V_0, the larger the output current and so is the output voltage. For the higher voltage, the time of pulse generation moves relatively ahead. The reason is that the higher the initial energy, the faster the metal heating process, and the earlier the explosion time, and the earlier the pulse generation time.

When the inductive storage L_R is, respectively, 2μH, 5.4μH and 9.0μH, the output current will decrease in turn. However, the output voltage is relatively low in the first case, and close in the last two cases. Again, the larger the conductor cross-sectional area, the larger the output current and voltage amplitude during a normal explosion process, and with the increase in the cross-sectional area, the time from conductor heating to explosion will become longer (under the condition that parameters such as initial energy are identical), and the pulse generation time will postponed accordingly.
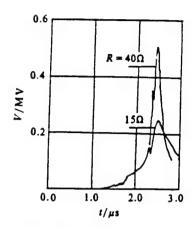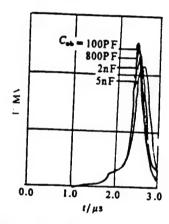
Fig.3 The affection of load to voltage
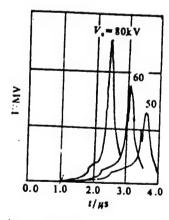

Fig.4 The affection of sharping capacitance to voltage

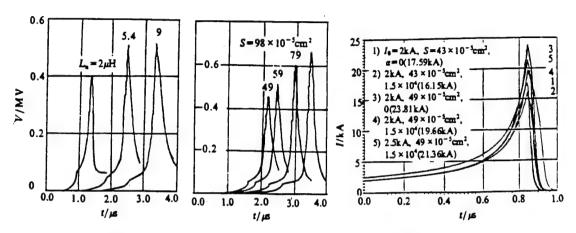Fig.5 The affection of charging voltage V_s to voltage

78

Fig.6 Affection of inductive storage Fig.7 Affection of cross–sectional Fig.8 Output current of MFCG
L_a to voltage   areas to voltage   (carrying EEOS)

In the simple MFCG model, the effect of magnetic leakage, initial current as well as the cross-sectional area of different conductors, respectively, are taken into account as shown in Figs. 8 and 9. At the same time, the initial calculation is conducted without EEOS. Fig. 10 shows the results of output current in the four scenarios. While the equivalent electric circuit is indicated in Fig. 11, where R_H can be considered as a dissipated resistance (5mΩ).

It can be found from Figs. 8 and 9 that when magnetic leakage is considered, the current and voltage output will decrease (curve 1 vs curve 2, curve 4 vs curve 5); with an increase in initial current, the current and voltage will accordingly increase (curve 4 vs curve 5). It is also known through comparison with Fig. 11 that when the initial current is 2kA and without consideration of the magnetic leakage, the current output is 23.81kA (an ideal explosion condition) with EEOS load, and the output current is 29.78kA without EEOS load, the increase being 20%. When the initial current is 2kA and the magnetic leakage is considered ($\alpha=1.5\times10^4$), the output current

79

with EEOS loading is 16.15kA(an ideal explosion condition), and without EEOS, the output current is 23.29kA, with an increase of 31%. When the inital current is 2.5kA and the magnetic leakage is considered, the output current is 21.36kA (an ideal explosion condition) with EEOS load, and without EEOS, the output current is 29.11kA, with an increase of 27%.
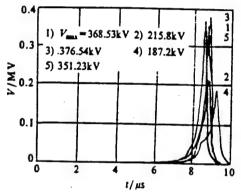
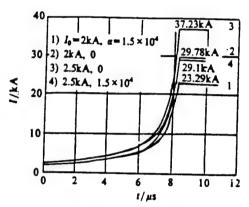Fig.9 voltage on conductor (carrying EEOS), curve parameters see Fig.8
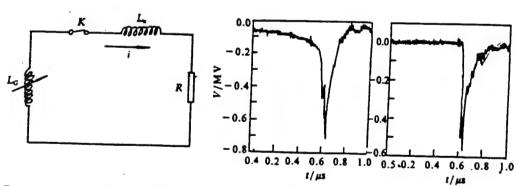
Fig.10 output current of MFCG (not carrying EEOS)

Fig.11 scheme of MFCF model

Fig.12 conductor voltage   Fig.13 load voltage

Through calculation of the capacitor model and simple MFCG model, it is found that when the power conditioning system is operated, there are optimal system parameters, under which ideal

output results can be accomplished. While under different experiment environments, these parameters are different. This should be adjusted through experiments. In the calculation of the simple MFCG model, the output results appear entirely different with or without EEOS load, which also is related to the degree of magnetic leakage. In our simple calculation, the output current decreases from 20 to 31% between two cases: without considering magnetic leakage ($\alpha=0$) and considering magnetic leakage (linear relation $K=\alpha t$, $\alpha=1.5 \times 10^4$).

3. Conclusions

Together with the simulation computation, a series of experimental studies were conducted of the pulsed power conditioning system and the magnetic flux cumulation generator, and the experimental results proved to conform to the theoretical analysis. The experimental results will be reported in specific papers and therefore will not be detailed here.

Figs. 12 and 13 show a typical experimental result (the signal was recorded with a TDS648 digital oscillograph). The conditions for the experiment were as follows: a capacitor group was taken as initial energy, the capacitance was 1.875µF, the sharpening capacity was 100pF, the initial charging voltage was 80kV, and the cross-sectional area of conductor was $98 \times 10^{-5} cm^2$.

Fig. 12 shows the voltage waveform on two ends of the conductor, while Fig. 13 indicates the voltage waveform on two ends of the operational load. By comparing with the simulation calculation, it is known that these two pulse waveforms are generally in conformity. However, the amplitude in the calculations is approximately 10% smaller than in the experimental results. The major reason for this difference is that the effect of the circuit distributive parameters was neglected during the calculation; instead, some empirical

parameters were somehow used. This should be adjusted in response to different experiment conditions. The leading edge of voltage at the end of the load is approximately 80ns, which is an relatively ideal result. From the comparison between the numerical simulation and experiments, the following conclusions can be derived:

(1) The calculations are in agreement with the experimental results, and the established models and calculation methods are reliable, which can be applied in practical performance as a reference, and can also be used to guide the development of experimental studies.

(2) Because of the limited space, the calculations of the T. J. Tucker model are not available in this paper. However, practical performance suggests that the result of that theoretical model has a significant reference value in system engineering design.

(3) With the capacitor group as initial energy, we can conduct systematic research on individual parameters of the pulsed power conditioning system in an attempt to select the matching running parameters. The desirable running parameters include: operational load 40Ω, sharpening capacity 100pF, and inductive storage 5.4μH. To improve the output level, the initial energy of the capacitor is required to be enhanced, and the cross-sectional area of the conductor should be enlarged, too. These parameters can be selected based on specific requirements.

(4) The magnetic flux cumulation generator that we used operates for a long period of time (6-8μs), and is required to output intense current (~30kA). Yet the output voltage is not that high, and the leading edge was relatively poor, which results in low efficiency in energy conversion to the load.

Nevertheless, if combined with a proper pulsed power conditioning system, voltage pulses with an ideal high amplitude and steep leading edge can be achieved and applied in various operational loads. But it is necessary to understand that this can only be realized at the expense of losing part of the energy and lowering the output current.

(5) In the study of the pulsed power conditioning system, it is known that an optimal matching between the output performance of the system and the running parameters is vital. To reach this goal, much needs to be done in theoretical research and experiments. Thus, the establishment of a related database and computer programs is highly recommended. This is also a major focus in our future endeavor.

REFERENCES

1   Tucker T J. A theoretical Model of the Resistance Behavior of Exploding Wire. SC−RR−71−0739, January 1972

2   Tucker T J et al. EBWI: A Computer Code for the predietion of the Behavior of Electrical Circuits containing Exploding Wire Elements. SAND−75−0041

3   Azarkevich E I et al. *Dokl. Akad. Nauk SSSR.* 1991, 319:352

4   AZarkevich E I et al. Generation of Microwave Radiation with the Aid of High explosive. Preprint. Chernoglovka, 1992 (Russian)

5   Burtsev V A et al. Electrical Explosion of Wires. Moscow, Energoatomizdat, 1990 (Russian)

6   Zherlitsin A G et al. High Voltage Pulse Generation Using an Explosive Magnetic Generator with Axis Initiation. MG−4, 1986

This paper was received for editing on July 24, 1995, and the edited paper was received on July 20, 1996.

NUMERICAL CALCULATION OF FOCUSED HIGH POWER
LASER BEAMS IN ATMOSPHERIC PROPAGATION

Xie Shumao, Lei Guangyu, and Zheng Shaotang

Institute of Applied Physics and
Computational Mathematics
P.O. Box 8009
Beijing 100088

ABSTRACT: Nonadaptive coordinate transformations are
applied to the basic equations for the simulation of
thermal blooming of focused high-power beams propagating
through the atmosphere in the report. The results show
that the accuracy and speed of the computation can be
improved efficiently. But it is difficult to calculate
the field near the focal plane because of the defocusing
of the thermal blooming. Modified nonadaptive changes
are presented in the paper which overcome the disadvantage
of the old nonadaptive changes, and has proved to be more
efficient in the improvement of accuracy and speed of
computation, and reduction of computer memory.
KEY WORDS: nonadaptive coordinate, focus, thermal blooming.

0. Introduction

A high power laser beam, while propagating through the
atmosphere, can generate self-defocusing, i.e., thermal blooming
phenomenon due to the absorption by the medium. The mathematical

methods used to simulate thermal blooming include: differential method, integration method, and the fast Fourier transform method (FFT)[1]. These methods have proven to be extremely effective while applied in calculating the thermal blooming of collimated beams, but in calculating the focused beam, their accuracy and speed will decrease due to two reasons. The first reason is that the high frequency oscillations that occurred in the focused-beam phase tends to exceed the sampling frequency of the computational mesh, while the second reason lies in the fact that as the transverse dimension of the focused beam continuously decreases during propagation, the number of meshes in the beam is growing smaller.

There are many ways to improve the accuracy and speed of computational handling of the thermal blooming of the focused beam. Among these ways, a nonadaptive coordinate transformation has proven to be an extremely effective technique[2]. This paper introduces this nonadaptive coordinate transformation technique as well as its defects. Also, a modified nonadaptive coordinate transformation technique is proposed in this paper to show that the modified technique can provide more accurate and faster computation with reduced computer memory.

1. Nonadaptive Coordinate Transformation Technique

The basic equations for studying thermal blooming are[3]:

$$\begin{cases} \nabla_\perp^2 \psi + 2ik \dfrac{\partial \psi}{\partial z} - \dfrac{2k^2}{n_0} \left| \dfrac{\partial n}{\partial T} \right| T\psi = 0, \\ \dfrac{\partial T}{\partial t} + u_\perp \cdot \nabla_\perp T = \dfrac{\alpha}{\rho c_p} I \end{cases} \tag{1}$$

where ψ is field amplitude; $k=2\pi/\lambda$ is the refractivity of unperturbed medium; T is temperature perturbation value; $u_\perp$ is wind speed perpendicular to the propagation direction; $I=\psi\psi^*$ is light intensity; α is the absorption coefficient of medium; α is the density of unperturbed medium; c_p is specific heat under fixed pressure.

85

For Eq. (1), the transverse dimension is scaled with the initial beam radius α, while the propagation direction is scaled with $k\alpha^2$: $x'=x/\alpha$, $y'=y/\alpha$ and $z'=z/k\alpha^2$; in phase transformation, the high frequency oscillation at the phase factor is eliminated so that the transformed field becomes smooth and easy to calculate, $\psi(x', y', z')=D^{-1/2}\exp\{i[(x'^2+y'^2)/2](d\ln D^{1/2}/dz')-i\,\text{arctg}[z'/(1-\delta z')]$ $\cdot\psi_1(x',y',z')$, where $D(z')=(1-\delta z')^2+z'^2$, $\delta=1/f'$ and $f'=f/k\alpha^2$. By scaling the transverse dimension with the beam radius in the beam propagation through vacuum $D^{1/2}$, the actual computational mesh varies with the variation of the beam dimension: $\tilde{x}=x'/D^{1/2}$, $\tilde{y}=y'/D^{1/2}$, $\psi_2(\tilde{x},\tilde{y},z')=\psi_1(x',y',z')$; in the strong light intensity zone, a small propagation step is automatically selected as $d\tilde{z}/dz'=1/D(z')$, $\psi_3(\tilde{x},\tilde{y},\tilde{z})=\psi_2(\tilde{x},\tilde{y},z')$. Following transformation, equation group (1) is converted to

$$\left\{\begin{array}{l} \tilde{\nabla}_\perp^2\psi_3+2i\dfrac{\partial\psi_3}{\partial\tilde{z}}+[(2-\tilde{x}^2-\tilde{y}^2)-\dfrac{2k^2a^2D}{n_0}\left|\dfrac{\partial n}{\partial T}\right|T]\psi_3=0 \qquad (2a)\\[4mm] \dfrac{\partial T}{\partial t}+\dfrac{1}{a\sqrt{D}}u_\perp\cdot\tilde{\nabla}_\perp T=\dfrac{a}{\rho c_p}\dfrac{I_1}{D} \qquad (2b) \end{array}\right.$$

where $I_1=\psi_3\psi_3^*$. Then the initial field distribution $\psi(x,y,z=0)=$ $=\psi_0\exp[-(x^2+y^2)/a^2-ik(x^2+y^2)/2f]$ is converted to $\psi_3(\tilde{x},\tilde{y},\tilde{z}=0)=$ $=\psi_0\exp[-(\tilde{x}^2+\tilde{y}^2)]$ after transformation.

In solving equation group (2) numerically, Eq. (2a) is first transformed so that the FFT technique can be applied

$$\psi_3(\tilde{x},\tilde{y},\tilde{z})=\psi_4(\tilde{x},\tilde{y},\tilde{z})\exp\left\{-\dfrac{1}{2}\int_{\tilde{z}_0}^{\tilde{z}}\left[\tilde{x}^2+\tilde{y}^2-2+\dfrac{2k^2a^2D}{n_0}\left|\dfrac{\partial n}{\partial T}\right|\right]T\,dz\right\} \qquad (3)$$

where z_0 is a constant. It is confirmed that Eq. (2a) can be converted to[1,4]

$$2i\dfrac{\partial\psi_4}{\partial\tilde{z}}+\bar{H}(\tilde{z})\psi_4=0$$

$$(4)$$

where the mean value $\bar{H}(\tilde{z})$ can be selected in two ways: $\dfrac{1}{2}[H(\tilde{z})+H(\tilde{z}+\Delta\tilde{z})]$ or $H(\tilde{z}+\dfrac{\Delta\tilde{z}}{2})$. The operator $H(\tilde{z})$ is

defined as

$$H(\bar{z}) = \exp\left\{ +\frac{i}{2}\int_{z_0}^{z}\left[\tilde{x}^2 + \tilde{y}^2 - 2 + \frac{2k^2a^2D}{n_0}\left| \frac{\partial n}{\partial T}\right| T \right]dz' \right\}\tilde{\nabla}_\perp^2 \cdot$$

$$\cdot \exp\left\{ -\frac{i}{2}\int_{z_0}^{z}\left[\tilde{x}^2 + \tilde{y}^2 - 2 + \frac{2k^2a^2D}{n_0}\left| \frac{\partial n}{\partial T}\right| T \right]dz' \right\}$$

where the second mean value of $\bar{H}(\bar{z})$ is selected, and Z_0 is evaluated as $\bar{z} + \Delta\bar{z}/2$, then $\bar{H}(\bar{z}) = \tilde{\nabla}_\perp^2$. Eq. (4) is converted to the in-vacuo propagation equation

$$2i\frac{\partial\psi_4}{\partial\bar{z}} + \tilde{\nabla}_\perp^2\psi_4 = 0 \tag{5}$$

To summarize, to solve ψ_3, we should first eliminate the nonlinear phase of the field at $\bar{z}$ using Eq. (3), and then solve the field that propagates from $\bar{z}$ to $\bar{z} + \Delta\bar{z}$ using Eq. (5), and finally add the phase factor using Eq. (3).

2. Numerical Calculation

Given $\lambda = 3.8\mu m$, $\alpha = 25cm$, $\alpha = 0.14 \times 10^{-5} cm^{-1}$ $u = 25m/s$, $I_0 = 256W/cm^2$, $f = 2.5km$, initial field distribution $\psi = \psi_0\exp[-(x^2+y^2)/a^2 - ik(x^2+y^2)/2f]$, thermal distortion number $N_D = 109.5$.
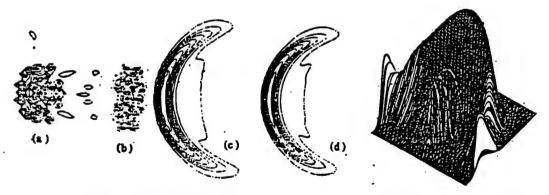

Fig.1 Isointensity contours

Fig.2 Intensity near focal plane

Fig. 1 shows isointensity contours derived through directly solving equation group (1) (the following description is focused on the isointensity contours alone except for special remarks), where the sample points, respectively, are N=64, 128 and 512, corresponding to Fig. 1(a), (b) and (c) respectively. The calculation proved to be inaccurate at N=64 and 128, and the calculation was accurate only when N=512. Fig. 1(d) represents calculations based on the nonadaptive coordinate changes with sample point N=64 and δ=41.3.

The calculations in Fig. 1(c) and (d) suggest that the nonadaptive coordinate transformation technique can be used to improve the accuracy and speed of computation but suffers from two significant defects: one defect is that the boundary of the shrinking mathematical mesh collides with the defocused beams due to thermal blooming during propagation computation, and the collision will cause numerical instabilities[5] as shown in Fig. 2. In this case, N=128, and δ=41.3. In order to avoid numerical instabilities, buffer length L must be increased, and to ensure a stable size of computational mesh, sample points N must be increased, as well. The other defect is that it is difficult to accurately calculate the field amplitude near the focal plane, which requires an ever decreasing longitudinal propagation step $\Delta z'$, i.e., an extremely great number of longitudinal propagation steps N_z. Because of the foregoing two reasons, the speed of computation was greatly reduced in calculating some interesting models, and the computer memory was also highly burdened.

To overcome the defects in the original transformation technique, we introduced two parameters f'_1, f'_2 and made them satisfy $1/f'=1/f'_1+1/f'_2$. Following these procedures, the initial distribution of the focused Gaussian beam (before transformation) was:

$$\psi(x',y',z'=0)=\psi_0 \exp\left[-(x'^2+y'^2)-\frac{i(x'^2+y'^2)}{2f'_1}-\frac{i(x'^2+y'^2)}{2f'_2}\right] \quad (6)$$

Let $\delta_1 = 1/f_1'$, and $\delta_2 = 1/f_2'$, Eq. (2) is converted to

$$\psi(x',y',z') = D^{-1/2} \exp\left[-i\frac{x'^2+y'^2}{2}\frac{d}{dz'}\ln D^{1/2} - i\,\mathrm{arctg}\,\frac{z'}{1-\delta_1 z'}\right]\psi_1(x',y',z') \tag{7}$$

where $D(z') = z'^2 + (1+\delta_1 z')^2$. Then, the initial distribution of $\psi_1(x',y',z')$ was selected as follows:

$$\psi_1(x',y',z'=0) = \psi_0 \exp\left[-(x'^2+y'^2) - i(x'^2+y'^2)\delta_2/2\right] \tag{8}$$
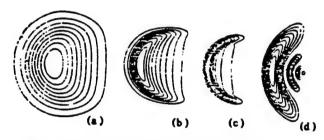
Fig.3 Isointensity contours on varied planes. $N = 512$
3 (a) $z = 1.125$km. 3 (b) $z = 1.625$km. 3 (c) $z = 1.875$km. 4 (d) $z = 2.5$km
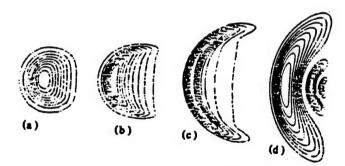
Fig.4 Isointensity contours on varied planes
(a) $z = 1.125$km. $N = 64$, $\delta_1 = 40.9$;　(b) $z = 1.625$km. $N = 64$, $\delta_1 = 40.9$
(c) $z = 1.875$km. $N = 128$, $\delta_1 = 34.4$;　(d) $z = 2.5$km. $N = 128$, $\delta_1 = 34.4$

Fig. 3 shows the calculations in solving equation group (1) with the number of sample points 512x512. Fig. 4 is calculations based on the modified nonadaptive coordinate transformation technique, with the number of sample points 64x64 in Fig. 4(a) and (b), and 128x128 in Fig. 4(c) and (d).

Fig.5 Isointensity contours on focal plane

In addition, the modified nonadaptive coordinate transformation technique can also be used to improve the numerical instability with a great thermal distortion number. When the thermal distortion number N_D increased to 237, the direct solution method may easily produce numerical instability (see Fig. 5a, sample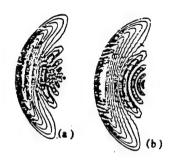 points N=512), while with the modified technique, numerical instability could be avoided (see Fig. 5b, the sample points N=256, δ_1=31.8).

To summarize, as long as the parameter $\delta_1(\delta_2)$ is properly chosen, the buffer area L and the number of sample points can be evaluated as small as possible in calculating either the field near the focal plane or the thermal distortion number N_z. In this case, the speed and computational accuracy can be effectively improved, and the computer memory can be reduced.

3. Analysis and Discussion

Tables 1 and 2, respectively, compare the vacuum diffraction and thermal blooming calculations using the direct solution method (briefly referred to as method 1) and the modified nonadaptive coordinate transformation technique (briefly referred to as method 2).

Table 1 shows the vacuum diffraction beam of the central values and their relative errors derived from the two algorithms, the computing mesh is selected as N=128, 256 and 512, respectively, for a comparison. It can be seen from the results shown in this Table that the computational accuracy is even higher in method 2 at N=128 than in method 1 at N=512, while the relative error of central light intensity is only 0.23% in method 2. Therefore, with method 2, it is enough to select the number of transverse computational mesh points as N=128.

Table 2 shows the thermal blooming calculations conducted with the two algorithms, where $I_r=I_a/I_0$; I_a is the maximum light intensity at the focal plane; I_0 is the central light intensity of vacuum diffraction; y_a is the y-coordinate value of the maximum light intensity: $y_a=0.0$ for uniform atmospheric thermal blooming. It can be seen from the Table that in method 1, when $N_D=109.5$, the calculation is unstable at N=128 and 256 (because $y_m \neq 0.0$) , and the calculation is stable at N=512, while in method 2, the calculation is already stable at N=128, and the computational accuracy is similar to that in method 1 at N=512. Once the thermal blooming strengthens until the thermal distortion number N_D reaches 237.0, the calculation made with method 1 is stable at N=512 but with a greater error, while method 2 is already stable at N=256 with a much smaller error.

TABLE 1. Comparison of In-vacuo Diffraction Calculation
with Two Algorithms

N	algorithm 1		algorithm 2		
	I_a	ξ	I_a	ξ	
128	1505.89	11.9%	1708.32	0.23%	
256	1648.6	3.5%	1708.91	0.11%	
512	1696.64	0.7%			

I_a is isointensity at centre. ξ is relative error.

TABLE 2. Thermal Blooming Calculations with Two
Algorithms

N	$N_a = 109.5$			$N_a = 237.0$		
	$I_r = 1$	$I_r = 2$	theory	$I_r = 1$	$I_r = 2$	theory
128	0.0174 $y_a = -\Delta x$	0.011 $y_a = 0.0$		0.00628 $y_a = -5\Delta x$	0.00105 $y_a = -\Delta x$	
256	0.0104 $y_a = -2\Delta x$		0.015	0.00427 $y_a = -7\Delta x$	0.00337 $y_a = 0.0$	0.0032
512	0.0175 $y_a = 0.0$			0.00734 $y_a = 0.0$		

$I_r = I_m/I_s;$ I_m is max $-$ isointensity on focal plane.

In selecting parameter δ_1, the thermal blooming effect can lead to beam divergence acting like a "thermal lens", and the focal length of this lens[6] $f_a = \pi k D^2 / \sqrt{2} N_D$; D is initial beam diameter; the phase distortion variable $N_D = 4\sqrt{2} (-n_T) \cdot k\alpha P z / (\rho c_p v D)$.

$k = 2\pi/\lambda$ is wave number; α is absorption coefficient of medium; P is total laser power; z is propagation distance;

ρ is density of medium; c_p is specific heat under fixed pressure; v is wind speed.

Let $f_2' = f_a' = f_a/ka^2$ and satisfy $1/f = 1/f_1' + 1/f_a'$, , then the parameter $= \gamma Fr$. $\gamma = (f_a' - f')/f_a' = (f_a - f)/f_a$, $\delta_1 = (f_a' - f')/f'f_a' = \gamma F_r$. and Fresnel number $Fr = ka^2/f$.

4. Conclusions

In this paper, the authors solved the thermal blooming problem that occurs in the atmospheric propagation of focused high power laser beams using the nonadaptive coordinate transformation technique. The calculations indicated that this technique proved to be effective in improving computational accuracy and speed.

However, this technique has its own severe defects. On the one hand, due to thermal blooming, the defocused beam will

collide with the boundary of the mathematical mesh and cause computation instability. In this case, it is necessary to increase the computational buffer area L and the mesh number N. On the other hand, since it is extremely difficult to calculate the field near the focal plane, an extremely large number of propagation steps N_z is required, and with an increase in L, N and N_z, the speed of computation will inevitably decrease, and the computer memory will be enlarged.

To overcome these defects, the authors proposed a modified technique. The calculations suggest that with this technique, as long as parameter δ_1 is properly selected, buffer area L and the number of sample points N can be selected as small as possible, and the number of propagation steps N_z can be greatly decreased in computing either the field near the focal plane or the great thermal distortion number N_D. As a result, the accuracy and speed of computation can be effectively improved, and the computer memory can be reduced.

REFERENCES

1   Walsh J L and Clrich P B. Laser Beam Propagation in the Atmosphere. edited by J. W. Strohbehn. New York, 1978, 294
2   Ulrich P B. Naval Res. Lab. Rept. 1971.7382
3   Koniaeu P A. Lukin V P. Appl Opt. 1985, 24 (3): 415
4   Bradley L C. Herrmann J. MIT Lincoln Lab. Rept. LTP – 10, 1971
5   Fleck J A. Jr. Morris J R and Feit M D. Appl Phys. 1976, 10: 129
6   Gebhardt F G. SPIE. 1990, 1221: 2

FITTING ERROR IN DIRECT-TILT
WAVEFRONT RECONSTRUCTION

Wang Yingjian, Wu Yi, and Gong Zhiben

Anhui Institute of Optics and
Fine Mechanisms
China Academy of Sciences
Hefei 230031

ABSTRACT: Using numerical simulation, the fitting
error is calculated in the adaptive optics phase
compensation for the turbulent effect of laser
propagation in the atmosphere. The results show
that the fitting error of the adaptive-optics
system is 1.24 times of that calculated using the
least-squares-fit method.
KEY WORDS: adaptive optics, fitting error.

0. Introduction

A fitting error is one of the most critical errors [1] of an
adaptive-optics system in compensating the wavefront distortion
due to the turbulence effects of light propagation through the
atmosphere. The fitting error is an error between the
deformable- mirror reconstructed wavefront and the actual-beam
distorted wavefront based on the wavefront reconstruction
calculation of the wavefront information detected using a
wavefront sensor. This error is normally expressed in variance.

94

In references [1] and [2], given a known beam wavefront distortion, the respective authors carried out a least-squares-fit for the beam wavefront distortion using a deformable mirror, and after making a theoretical analysis of the so-called fitting error, directly regarded the fitting error as the wavefront reconstruction error.

The results of the analysis given in reference [1] suggest that if only the atmospheric turbulence can satisfy the Kolgomorov spectrum, the fitting error from the deformable mirror in which drivers are uniformly distributed will be

$$\sigma_{fu}^2 = K(d/r_0)^{5/3} \qquad (1)$$

where d is average interval among drivers in the deformable mirror; r_0 is the transverse coherent length of atmospheric turbulence; and K is wavefront fitting coefficient. For the Gaussian influential function, when the coupling coefficient is 0.15, K will be 0.349[1]. However, in actual adaptive-optics phase compensation for light wave propagation through the atmosphere, the beam phase can hardly be derived directly; instead, it can be obtained through indirect wavefront reconstruction after beam wavefront tilt (or curvature) is measured.

In wavefront reconstruction calculations using the model technique, wavefront Zernike polynomial fitting should be conducted first using the wavefront-tilt least variance before the reconstructed wavefront can be calculated through the least-squares-fit method. In this case, obviously, the fitting error is assumed to be greater [3] than the estimated fitting error value in reference [1]. With numerical simulation, the authors further calculated quantitatively the fitting error derived from the direct tilt wavefront reconstruction algorithm.

1. Simulation of Direct Tilt Wavefront Reconstruction

95

Reference [3] detailed the numerical model of the adaptive-optics system, including simulation of Hartmann wavefront detection, model wavefront-reconstruction algorithm, etc. In this paper, the direct-tilt wavefront reconstruction algorithm was applied.

Let the tilt in the x and y directions of the beacon wavefront at the l-th subaperture of the Hartmann wavefront sensor be $T_{sx}(1)$ and $T_{sy}(1)$, and let the tilt of the reconstructed wavefront at the corresponding subaperture of the deformable mirror be $T_x(1)$ and $T_y(1)$, i.e.,

$$T_x(l)=\sum_{n=1}^{N_d}d_n\iint_l R'_x(n,x,y)\,dxdy/A_l\,,\quad T_y(l)=\sum_{n=1}^{N_d}d_n\iint_l R'_y(n,x,y)\,dxdy/A_l \qquad (2)$$

where R'_x and R'_y) are the differentiation of the influential factor $R(n, x, y)$ toward x and y; N_d and d_n, respectively, are the number of drivers in the deformable mirror, and the driving volume of the drivers; the integration area is mirror surface of the l-th subaperture; A_l is the area of subaperture. The variance between the tilt of the detected wavefront and the tilt of the reconstructed wavefront will be

$$\sigma_T^2=\sum_{l=1}^{N_h}[T_{sx}(l)-T_x(l)]^2+\sum_{l=1}^{N_h}[T_{sy}(l)-T_y(l)]^2 \qquad (3)$$

N_h is the number of subapertures of the Hartmann wavefront sensor. By taking the driving volume of drivers d_n as a variable, and solving, respectively, the differentiation of σ_T toward $d_n(n=1,\ldots,N_d)$, and letting it be zero, i.e., the least-squares-fit condition, N_d number of equations can be derived, which are expressed in the matrix

$$\{[R_{n,l}]_x[R_{l,n}]_x+[R_{n,l}]_y[R_{l,n}]_y\}[d_n]=[R_{n,l}]_x[T_{sx}(l)]+[R_{n,l}]_y[T_{sy}(l)] \qquad (4)$$

where

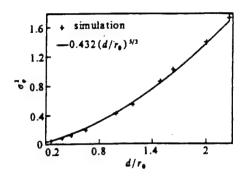$$[R_{n,l}]_x=\iint_l R'_x(n,x,y)\,dxdy/A_l\,,\qquad [R_{n,l}]_y=\iint_l R'_y(n,x,y)\,dxdy/A\,,$$

$[R_{ln}]_x$, $[R_{ln}]_y$ are the transposed matrixes of $[R_{nl}]_x$ and $[R_{nl}]_y$; while $[T_{sx}(1)]$ and $[T_{sy}(1)]$ are the detected tilt matrixes. Thus, by solving the linear equations, the driving volume of drivers in the deformable mirror can be obtained.

2. Discussion

With numerical simulation programs designed for laser beam atmospheric propagation and its adaptive-optics phase compensation, we calculated the adaptive-optics phase compensation for turbulence effects of laser propagation through the atmosphere, and analyzed the fitting error derived from the direct-tilt wavefront reconstruction technique, and its effect on the laser far-field Strehl ratio. We utilized the phase shield technique in calculating laser propagation, and the inverse spectrum algorithm in dealing with the turbulence phase shield[3].

The calculation parameters included: both the main laser beam and beacon light being finite plane waves with a wavelength $\lambda = 1.315 \mu m$, transmission aperture D=0.5m, propagation distance 3km; the turbulence spectrum being the Von-Karmann spectrum with external dimensions L_0=10m and internal dimensions l_0=5mm; the number of units in the adaptive-optics system being 37, the drivers in the deformable mirror being in uniform distribution; for convenience in comparison, a Gaussian influential factor was also adopted with coupling coefficient 0.15, and free deformable mirror edge.

In our numerical calculation, the laser beam propagation 3km was calculated first before the far-field distribution was computed with the Fraunhofer integration formula, and eventually, the far-field Strehl ratio of laser beam was derived.
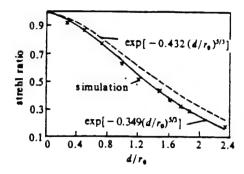
97

Fig.1 The residual wavefront variance vs d/r_0 Fig.2 The far field Strehl ratio of laser beam vs d/r_0

Fig. 1 shows the direct-tilt fitting error versus d/r_0. "+" stand for numerical calculations; the solid line is a fitting line based on Eq. (1); K=0.432. It is found from Fig. 1 that the direct-tilt fitting error can also be described using Eq (1), and its fitting coefficient is 1.24 times that of the fitting error calculated using the least-squares-fit technique.

Since in the model wavefront reconstruction calculation, the tilt least variance is also required in wavefront model fitting, its fitting error is basically equal to that derived from the direct-tilt technique[3]. Thus, the indirect fitting error obtained in an actual system is greater than that based on the least-squares-fit technique.

According to reference[1], in adaptive-optics phase compensation for turbulence effects , the Strehl ratio of the laser beam and its residual wavefront variance σ_φ can satisfy

$$S=\exp(-\sigma_\chi^2+\sigma_\varphi^2), \quad \sigma_\varphi^2=\sigma_{sen}^2+\sigma_F^2+\sigma_{temp}^2+\sigma_{iso}^2 \tag{6}$$

where σ_χ^2 is amplitude fluctuation variance; σ_F^2 is fitting error; under our calculation conditions, the error in the finite zone of the system σ_{temp}^2 the anisoplanatism error σ_{iso}^2 and the detected wavefront error σ_{sen}^2 are all equal to zero. Therefore, the major effect on the Strehl ratio originates from the fitting error, i.e., $\sigma_\varphi^2=\sigma_F^2$. The amplitude fluctuation error can be calculated using the formula presented in reference[1]. Fig. 2 shows a comparison between the numerical calculations on the far-field Strehl ratio of the beam and the coherent length of turbulence in the case of phase compensation,

and calculations based on Eq. (6), where "□" is numerical calculations; the solid line and dashed line are calculations based on Eqs. (1) and (6) at K=0.432 and 0.349. It can be seen from Fig. 2 that when K=0.432, the analysis results are in good agreement with the numerical calculations, while the fitting error derived from the least-squares-fit technique is obviously under-estimated, from which the Strehl ratio appears higher than in numerical calculations.

It is known from the foregoing calculations that in the adaptive-optics system that adopts wavefront tilt in carrying out wavefront reconstruction, the reconstruction error of wavefront distortion caused by atmospheric turbulence is 1.24 times the fitting error calculated using the least-squares-fit method.

REFERENCES

1   Tyson RK . Principles of Adaptive Optics. 1991, Academic Press, INC.
2   Hudgin RH. *J Opt Soc Am*. 1977, 67(3): 393~395
3   王英俭. 吴毅. 龚知本. 强激光与粒子束. 1994, 6(1): 59

PULSE STRUCTURE OF A FAR-INFRARED FREE-ELECTRON LASER

Ding Wu, Zhang Zhichou,
Shu Xiaojian, and Yao Jun

Institute of Applied Physics and
Computational Mathematics
P.O. Box 8009
Beijing 100083

ABSTRACT: With an INEX model, the start up and the
structure of optical pulse of CAFP FIR FEL are studied.
To counteract the effect of lethargy, the necessary
detuning of the cavity length, and precision and range
for adjusting cavity length are given. The gain, power,
pulse width and bandwidth are predicted. The pulse
structure different cavity length is investigated.
KEY WORDS: free-electron laser, detuning, lethargy effect,
pulse structure.

0. Introduction

To date, free-electron lasers(FEL) in the infrared and far-
infrared spectral ranges have advanced to a stage of maturity
with some unique features. In particular, the FELIX system
developed in The Netherlands can continuously change FEL
wavelength within a microsecond. Through adjusting the frequency
of the RF accelerator, dynamic detuning of cavity length can be
achieved, i.e., the optical pulse width can be changed over a

range of several-fold[1,2], which has provided satisfactory conditions for FEL applications.

Based on the theoretical design of the far-infrared FEL system developed by China Academy of Physics (CAEP), we studied, by using an integral numerical (INEX) simulation technique[3], i.e., numerical simulation based on the simulation calculations of accelerator and beam-current transmission line segment[4] as the initial value of the FEL segment, the laser lethargy effect and its start-up, provided a desynchronism curve, and proposed requirements for accuracy and range in adjusting cavity length. Additionally, we estimated significant parameters, such as optical wavelength, gain, power, pulse width, and bandwidth, and also studied the optical pulse shape, width, and spectrum versus cavity-length detuning value. All these served as a preparation for CAEP FEL experimentation and application.

1. Simulation Equations and Conditions

The CAEP FEL system is mainly composed of RF accelerator, beam current transmission line, plane waveguide, linearly polarized-plane magnetic wiggler, and optical cavity. We took the direction of electron beam propagation, optical cavity axis, wiggler axis, and plane waveguide axial line as the z-axis, and the plane with the wiggler magnetic field as the y-z plane, as well as the entrance of the wiggler (not including the transition area) as the point z=0.

The FEL coupled equation is of the KMR-type [5] coupled equation without considering the space electric charge effect. This equation deals with the propagation of electron beams and optical pulses in time and space, and also contains z and time variable. In fact, the electron motion is three dimensional-oriented, while the optical-field transverse distribution is taken as the base mode, namely the product of zero-order

Hermitian-Gaussian mode in the x-direction and one-order waveguide mode in the y-direction.

The WFELP program was designed in consideration of the effect of waveguide on the optical phase velocity and FEL resonance, the optical field, transverse constraints, and longitudinal slippage[6]. Concerning the chromatic stretching effect of waveguide on optical pulse wave packet, the optical wave packet can be written as:

$$a_s(z, t) = \int_{-\infty}^{+\infty} a_w(k, \omega) e^{i\omega t - ikz} d\omega \tag{1}$$

Since the group velocity has propagated over length L during the time $\tau = L\omega_c / k_c c^2$ in the z-direction, the wave packet can be changed to

$$a_s(z+L, t+\tau) = \int_{-\infty}^{+\infty} a_w(k, \omega) e^{i\Delta\Phi} e^{i\omega t - ikz} d\omega \tag{2}$$

$$\Delta\Phi = \frac{L}{k_c} \left(\frac{\omega\omega_c}{c^2} - kk_c \right) \tag{3}$$

where ω_c is FEL base frequency, k_c is the corresponding wave number in the waveguide[6]; the point-by-point mutual effect between FEL action and chromatic stretching of wave packets in the wiggler is ignored; each pass is given only a one-time consideration, and is subjected to a Fourier positive and inverse transform. According to the foregoing equation, L is twice the cavity length, and the chromatic stretching of the waveguide over the optical wave packet is taken into account.

Since the time scale of the RF accelerator is much larger than that of FEL, the number of simulating electrons derived from the PARMELA program calculation is overly small, that is to say, only 30- 40 electrons in one FEL wavelength, which is not enough to reflect the details of longitudinal change in electron distribution. Thus, the same electron distribution is designed for various electron beam groups in the FEL segment, and various

simulating-electron-state parameters (position, velocity, energy) in the entire micropulse derived from the calculations based on PARMELA program are taken as the initial value of simulating neutrons in the FEL fragment. At the same time, the transition area of the wiggler is assumed to be an ideal area for some of the electron longitudinal velocities adiabatically to be converted to transverse wiggler motion velocities without considering its effect on electron beam quality. Finally, the phase in the mass power potential formed by electrons in the optical field and wiggler field can be constituted using the static start-up method.

The simulation calculation parameters include: electron beam energy factor $\gamma=4.965$; beam current 10A, pulse length 20ps; the repetition frequency of micropulse 1.3GHz; macropulse length 4µs; wiggler period length 1.6cm; magnetic induction intensity 0.6T; number of periods 30; waveguide gap 0.5cm; cavity length 138cm; the radius of curvature of cavity mirror 82cm; the length of optical pulse is equal to the length of the electron beam pulse plus a length for slippage, respectively, in the front and at the back, both of which are designed in rectangular pulse distribution; the optical waist is at z=20cm; total losses in the optical cavity is 10%.

For the resonance wavelength and gain curve, the gain versus optical wavelength is calculated with the INEX method in stationary state (i.e., the relative slippage between the electron beam and optical pulse is not included). The maximum stationary-state small-signal gain is approximately 7.6 at $\lambda_r=504\mu m$; the gain width (FWHM) is approximately 3%; the uniform width is roughly 1/2N=2%; due to nonuniform widening yielded by energy dispersion and divergence, the gain width is increased by 50%. The electron beam quality can meet the FEL requirements.

2. Detuning of Cavity Length

The electron beam pulse length is $l_b = 0.6$cm. Since the waveguide can cause a decrease in group velocity, the slippage length s in the wiggler is smaller than 1.51cm in the absence of waveguide and reduced to 1.36cms. At this point, there is:
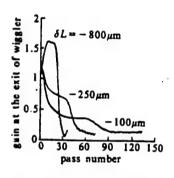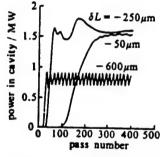
$$u = s/l_b = 2.3 \qquad\qquad (5)$$

Because of the severe lethargy effect[7], the cavity length needs to be slightly shortened to ensure an overlap between the gravity center of optical pulse and electron pulse. Fig. 1 shows the gain versus the Pass at the detuning of cavity length δL=-100, -250, and -800μm. Obviously, the gain of the first pass is disassociated with δL, while the plateau area in the curve should be considered. At this point, the optical pulse forms a so-called overmode structure[8], in which the stable gain G_{st} is subject to δL, and the length of the plateau area depends on the FEL saturation mechanism and δL value. As shown in Fig. 1, with an increase in $|\delta L|$, G_{st} increases, yet the length of the plateau area is shortened, and the time of saturation is ahead. Fig. 2 shows the development of the corresponding cavity length, which speeds up and is quicker to reach saturation with the increase in $|\delta L|$. Table 1 lists the detailed data, of which, P is the saturation value of the micropulse average power (averaged to l_b+s); N_p is the number of saturated passes; η is the extraction efficiency of electron number; P_p is the medium peak power of the optical micropulse; l_s is optical micropulse width (FWHM); F_p is the proportion of main frequency (with a width 1.52%) power in the overall power; λ_* is corresponding wavelength; Δ is spectral width (FWHM).

The desynchronism curve is shown in Fig 3, in which, the ordinate stands for saturation power, while in general experiments, the average power of a macropulse can be measured, in which one macropulse (4μs) contains over 400 passes. Thus, in the measured desynchronism curve, the peak appears a little up at

the left side and a little down at the right side. Because of the chromatic stretching effect of the waveguide on the optical pulse wave packet, the lethargy effect is somehow weakened, and the desynchronism curve becomes gentle and wider, and especially, the dropping tendency of the curve on the right side of the peak diminishes. Hence the waveguide can somehow helps stabilize the FEL operation.

From an overall consideration of the effect of δL on the gain, power and N_p, it was found that the proper cavity length detuning value is $-250\mu m$; the accuracy for adjusting the cavity length is required to be less than $50\mu m$, while the adjustment range is supposed to be greater than $1000\mu m$.
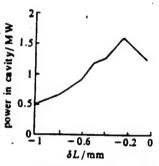

Fig.1 Gain vs pass number

Fig.2 Build–up of optical power

Fig.3 Desynchronism curve

Table 1 Results in different cavity lengthes

$-\delta L/\mu m$	50	100	200	250	300	400	600
G_x	0.25	0.37	0.62	0.72	0.84	1.04	1.36
P/MW	1.27	1.36	1.53	1.61	1.49	1.26	0.93
$\eta/\%$	0.62	0.66	0.75	0.79	0.73	0.62	0.45
N_p	209	118	72	61	55	45	35
P_p/MW	4.70	5.37	5.39	5.65	4.29	3.16	1.71
l_s/cm	0.45	0.40	0.45	0.45	0.50	0.55	0.70
$F_p/\%$	27.2	24.6	20.7	19.5	19.4	21.2	34.6
$\lambda_w/\mu m$	512	519	527	527	519	519	512
$\Delta/\%$	4.5	5.2	7.2	7.2	7.4	5.9	3.0

Table 2 Average values over a macropulse in different cavity lengthes

$\delta L/\mu m$	-50	-250	-600
P/MW	0.89	1.42	0.75
P_p/MW	2.86	3.88	1.09
l_s/cm	0.47	0.48	1.71
$F_p/\%$	25.9	28.3	51.3
$\lambda_w/\mu m$	519	519	512
$\Delta/\%$	5.1	3.2	1.9

3. Optical Pulse Width and Spectrum

Since an electron beam is subject to short pulses, severe slippage and waveguide, the development of its spectrum is relatively complex. This development mainly involves three processes: one is the process from self-radiation to the creation of FEL, longitudinal-mode purification and spectrum narrowing; this process is chosen because detuning the cavity length can speed up the competition of longitudinal modes. The second process is the super-radiation process of short pulses[9], i.e., in the optical pulse distribution, the first main peak (excited radiation FEL) is followed by one or several peaks (super radiation). The third process is the process of electron synchronized oscillation and sideband instability in the mass power potential[7,10], which causes the optical wavelength to drift to the long wave, and the spectrum to broaden. Among other aspects, the waveguide can not only decrease the group velocity and affect slippage[6], but can also cause the optical pulse wave packet to stretch, and its spectrum to become narrow[11].

The basic optical pulse is equivalent to the electron beam pulse width l_b. According to the limit of the Fourier transform, the spectrum width is π/l_b , from which, $\Delta \approx \lambda_s/2l_b \approx 4\%$. It is seen from Table 1 that the optical wavelength shifts by 21-4% to the long wave direction, which is equivalent to the gain width, and matches the general theoretical result.

The larger the proportion of the main frequency F_p, the larger the l_s, the wider the pulse, the smaller the Δ , and the narrower the spectrum. δL ranges from 150 to -400μm; P, η , P_p, l_s, $F_{p'}$ λ_s , and Δ basically remain unchanged; the optical pulse width l_s is approximately 0.5cm and spectrum width Δ is approximately 7%. This is because of two factors: one is that with increase in $|\delta L|$, the electron beam moves at the optical pulse and enlarges different sections of the optical

pulse, resulting in broadening the optical pulse width; the other factor is the fact that the waveguide can cause chromatic stretching of the optical pulse wave packet, and a narrower spectrum. While the gain and wave packet shape tend to interact and affect each other, these two factors act alternatively, coupled with the foregoing longitudinal mode competition, super radiation and sideband instability, resulting in a complex variation process of optical pulse width and spectrum width. Among the current available parameters of this system, the pass number is overly small, the longitudinal mode purification is not sufficient, cavity power is not high, the super radiation and sideband are not distinct, and the waveguide gap is large without apparent effect. Overall, with the increase in $|\delta L|$, the optical pulse width will become broader, and the spectrum will become narrower. This change may range over two to threefold.

Hence, in such short pulse non-intensive current systems, the optical pulse and spectrum are determined by $|\delta L|$. By taking advantage of this feature and through the cavity length detuning technique, different optical pulse lengths can be obtained, which provide conditions for FEL applications[1,2]. Fig. 4 shows the development of optical pulse under two cavity length detuning values. a and d are located in the stable gain plateau area as shown in Fig. 1, where the shape of optical pulse and peak position do not vary with pass, and form a so-called overmode stable structure[7,8]. b and e are situated near saturation, and enter the large signal area where the gain drops, the lethargy effect weakens, and optical pulse moves forward, and both the super radiation and sideband start to emerge. When $\delta L = -600\mu m$, under the joint effect of super radiation and synchronized accelerator oscillation, the limit ring effect appears[1,7,12], which is reflected as power-periodical oscillations in the macropulse as indicated in Fig. 2., and the buildup of the optical pulse is indicated as the oscillation within the dual peaks (Fig. 4e, f). The new peak is generated at the tail of the

pulse and constantly shifts forward due to the presence of desynchronism and the weakening of lethargy effect. On the other hand, since the previous old peaks slip out of the electron beam and become weak, dual-peak oscillation occurs, whose state and oscillation period depend on the gain, loss, slippage and δL value.

Under current conditions, it is difficult to measure the micropulse volume experimentally; instead, the macropulse average value is measured in most cases. As far as the macropulse average values of power, pulse width and spectrum are concerned, the pulse width and spectrum width are both derived from the FWHM value of the main peak. In two cases of a smaller $|\delta L|$, the average value of the macropulse is close to the value near the saturation as shown in Table 1, while in the event when $\delta L=-600\mu m$, the averaged pulse width in the macropulse can attain a value of 1.71cm, its spectral width is smaller than 1.9% and the proportion of the main frequency reaches 51% which is better than the value near saturation.
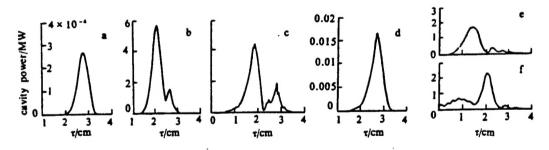

Fig.4 Development of optical micropulse, at a:20th, b:60th, c:400th pass with $\delta L=-250\mu m$; d:20th, e:60th, f:400th pass with $\delta L=-600\mu m$.

4. Conclusions

Under the current available parameters of CAEP FEL, through numerical calculations using the INEX method[3], the required cavity-length detuning value was found to be approximately

-250μm; the required accuracy for adjusting cavity length is smaller than 50μm; adjustment range is larger than 1000μm; optical wavelength is approximately 500μm; gain is roughly 70%; gain width is 3%; micropulse power is roughly 1MW; the average cavity power of macropulse is roughly 0.1MW; optical pulse width is roughly 0.5cm; spectral line is roughly 3%. Through adjusting the cavity length detuning value, the optical pulse width can be altered by several times above 0.5cm.

REFERENCES

1   Opets D. The FELIX User facilities. CCAST symposium/workshop on development and application of free electron laser. May 29—June 2, Beijing, China
2   Knippels G M H. *Nucl Instr and Meth*, 1994, A341: ABS26
3   束小建等. 强激光与粒子束, 1996, 8(2):286
4   吴中发, 王玉芝. 强激光与粒子束, 1995, 7(2):235
5   Kroll N M, Morton P L and Rosenbluth M N. *IEEE J*, 1981, QE17: 1436
6   Xiaojian Shu. *Optics Comm*, 1994, 105: 188
7   Colson W B, Reinieri. *J Phys Colloq*, 1983, 44(C1): 11
8   Dattoli G et al. *IEEE J*, 1981, QE17:1371
9   Moore G T, Piovella N. *IEEE J*, 1992, QE27:2522
10   束小建, 王泰春. 中国核科技报告, 1992, CNIC-00605, IAPCM-0020
11   Ciocci F. *Phys Rev Lett*, 1993, 73:928
12   Jarosynski D A et al. *Nucl Instr and Meth*, 1993, A331: 52

This paper was received for editing on July 25, 1995, and the edited paper was received on June 4, 1996.